Continental Shelf Research 98 (2015) 54–71

Contents lists available at ScienceDirect

Continental Shelf Research

journal homepage: www.elsevier.com/locate/csr

Research papers

Ocean acidification along the Gulf Coast and East Coast of the USA

Rik Wanninkhof [a,*], Leticia Barbero [a,b], Robert Byrne [c], Wei-Jun Cai [d], Wei-Jen Huang [d], Jia-Zhong Zhang [a], Molly Baringer [a], Chris Langdon [e]

[a] NOAA Atlantic Oceanographic and Meteorological Laboratory, 4301 Rickenbacker Causeway, Miami, FL 33149, USA
[b] Cooperative Institute for Marine & Atmospheric Studies, University of Miami, Miami, FL 33149, USA
[c] University of South Florida College of Marine Science, St. Petersburg, FL 33701, USA
[d] School of Marine Science and Policy, The University of Delaware, Newark, DE 19716, USA
[e] Rosenstiel School of Marine and Atmospheric Sciences, University of Miami, Miami, FL 33149, USA

ARTICLE INFO

Article history:
Received 6 November 2014
Received in revised form
26 February 2015
Accepted 27 February 2015
Available online 4 March 2015

Keywords:
Ocean acidification
Inorganic carbon system
Coastal ocean
Northern Gulf of Mexico
East Coast

ABSTRACT

As part of an effort to monitor changes in inorganic carbon chemistry of the coastal ocean, near-synoptic cruises are being conducted in the Northern Gulf of Mexico and along the East Coast of the United States. Here we describe observations obtained on a cruise in the summer of 2012 and compare them with results from a cruise following a similar track in 2007. The focus is on describing spatial patterns of aragonite saturation state (Ω_{Ar}). This parameter is an indicator of ecosystem health, in particular for calcifying organisms. The results show large-scale regional trends from different source waters at the northeastern and southwestern edges of the domain, along with the modulating effects of remineralization/respiration and riverine inputs. The broader patterns and changes over five years along the coast can be well described by the impacts of large-scale circulation, notably changes in source water contributions. Changes in the well-buffered Loop Current and Gulf Stream with high Ω_{Ar} impact the waters in the southern part of the study area. The less buffered southward coastal currents with low Ω_{Ar} originating from the Labrador Sea and Gulf of St. Lawrence impact the Ω_{Ar} patterns in the Northern regions. The expected 2% average decrease in Ω_{Ar} in the surface mixed layer due to increasing atmospheric CO_2 levels over the 5-year period is largely overshadowed by local and regional variability from changes in hydrography and mixed layer dynamics.

1. Introduction

Changes in the inorganic carbon chemistry of seawater due to invasion of anthropogenic carbon dioxide (CO_2) from the atmosphere is referred to as ocean acidification (OA). The increase of surface water CO_2 leads to a decrease in the buffering capacity of the ocean due to loss of carbonate ions (CO_3^{2-}) following the stoichiometry shown in Eq. (1).

$$CO_2 + CO_3^{2-} + H_2O = 2\ HCO_3^- \quad (1)$$

This decrease of CO_3^{2-} has a direct impact on the growth and survival of calcifying organisms. Other changes associated with increasing atmospheric CO_2 levels and uptake of the excess CO_2 by the ocean, such as increases in the hydrogen ion concentration and increasing partial pressure of CO_2, impact a variety of organisms as well (Wittmann and Portner, 2013).

Increases in surface water CO_2 levels dependably follow increasing atmospheric levels, particularly in the open ocean. While deviations from these trends can have impacts on global ocean carbon uptake on seasonal to interannual scales (Le Quéré et al., 2010; Takahashi et al., 2009; Wanninkhof et al., 2013), they generally do not have appreciable impacts on global OA trends within the current uncertainty of measurements. Locally, and particularly in the coastal ocean and nearshore, there are several confounding effects that can impact ocean acidification. These processes affect the inorganic carbon speciation shown in Eq. (1) and are often included in a broader description of OA. The processes effecting OA, and OA changes and trends in the coastal oceans must be monitored and understood as most of the commercial and recreational fisheries and aquaculture industries occur near the coast.

Effects that modulate the general trend of ocean acidification include respiration and remineralization of organic matter, releasing CO_2 in the aquatic environment (Cai et al., 2011). These processes are generally associated with oxygen drawdown, which in stratified waters can lead to hypoxia and have detrimental influences on ocean biota as well (Zhang et al., 2013; Rabalais et al., 2014). Upwelling of water with high CO_2 levels can have a

* Corresponding author.
E-mail address: rik.wanninkhof@noaa.gov (R. Wanninkhof).

http://dx.doi.org/10.1016/j.csr.2015.02.008

large effect on OA both as a direct influence and because upwelled CO_2-rich water is less buffered such that invasion of anthropogenic CO_2 causes an enhanced decrease in CO_3^{2-} (Feely et al., 2008; Harris et al., 2013). Continental contributions from rivers, swamplands, estuaries, and groundwater inputs can also have appreciable and variable impacts, and these effects are often measured along the salinity gradients from continental sources to the coastal ocean (Cai and Lohrenz, 2007; Cai et al., 2010; Huang et al., 2015; Liu et al., 2014; Salisbury and Green, 2008). Such impacts are expected to be particularly significant for rivers with low alkalinity and thus weak buffer capacity (Hu and Cai, 2013).

In response to the threats of ocean acidification and confounding factors, the Ocean Acidification Program (OAP) of the National Oceanic and Atmospheric Administration (NOAA) has been charged with setting up an ocean acidification monitoring network to quantify the increase in near surface water CO_2 (and decrease in pH) and associated changes in inorganic carbon speciation. As part of the observing scheme, dedicated research cruises are conducted to investigate the water column properties along select transects, and pertinent surface water characteristics are evaluated along the cruise track.

The second Gulf of Mexico and East Coast Carbon Cruise (GOMECC-2) took place on NOAA ship *Ronald H. Brown* from July 21 through August 13, 2012 with 8 cross-shelf transects in the Gulf of Mexico (GOM) and East Coast of the United States covering distinct biogeochemical regimes. The overall characteristics of the regions are described in Wang et al. (2013) based on the first GOMECC study in 2007. From the Louisiana line to the Cape Hatteras line (Fig. 1), the study region is bounded by the Loop Current, Florida Current, and Gulf Stream system. These waters serve as endmembers in coastal mixing dynamics and act as a conduit for northward movement of chemical constituents that originate from the adjacent coastal seas and gyres. To the north of Cape Hatteras, impacts of the Labrador Sea slope water and associated coastal jets prevail in coastal waters (Fratantoni and Pickart, 2007; Han et al., 2014). The data from the GOMECC-2 cruise are used to describe the state of the inorganic carbon system in this realm and, in combination with the GOMECC-1 data, are used to evaluate differences over the last 5 years. Our discussion is focused on the dynamics of the aragonite saturation state (Ω_{Ar}) as a prime indicator of OA. The GOMECC-2 data are used to show spatial distributions in this parameter, and with data from GOMECC-1 provide a comparison of Ω_{Ar} between the summers of 2007 and 2012.

While different organisms have varying sensitivities to the different forms of inorganic carbon, their sensitivities can often be categorized by the physical and chemical state of seawater, in particular Ω_{Ar}. The Ω_{Ar} is a primary control on calcifying rates and the mortality of calcifying organisms (Andersson, 2014; Waldbusser et al., 2015). The Ω_{Ar} can also serve as an indicator of the state of the inorganic carbon system, encompassing alkalinity (TAlk), total dissolved inorganic carbon (DIC), salinity, temperature and pressure effects.

The Ω_{Ar} is not measured directly but is calculated from observed variables. It is defined as the product of calcium and carbonate ion concentrations divided by the solubility product of the calcium carbonate mineral phase aragonite:

$$\Omega_{Ar} = [Ca^{2+}]\,[CO_3^{2-}]\,(K'_{Ar\ spP})^{-1} \quad (2)$$

where $[Ca^{2+}]$ is the total calcium concentration and is derived from salinity. It is based on the constancy of composition of major cations in seawater. The $[CO_3^{2-}]$ is the total carbonate ion concentration determined from two of the four measured inorganic carbon system parameters, and $K'_{Ar\ spP}$ is the apparent solubility product of the calcium carbonate mineral phase aragonite in seawater at a specified salinity, temperature and pressure. If Ω_{Ar} is less than one, the mineral phase is thermodynamically unstable.

Here we investigate the surface and subsurface patterns of Ω_{Ar} along the Gulf Coast and East Coast of the United States and factors that influence it. The sensitivity and uncertainty of the calculations are discussed. The geographical and temporal variations of Ω_{Ar} are presented along with the confounding effects of continental inputs and remineralization. Following Wang et al. (2013) the Gulf Stream is used as a demarcation in the coastal region up to Cape Hatteras,

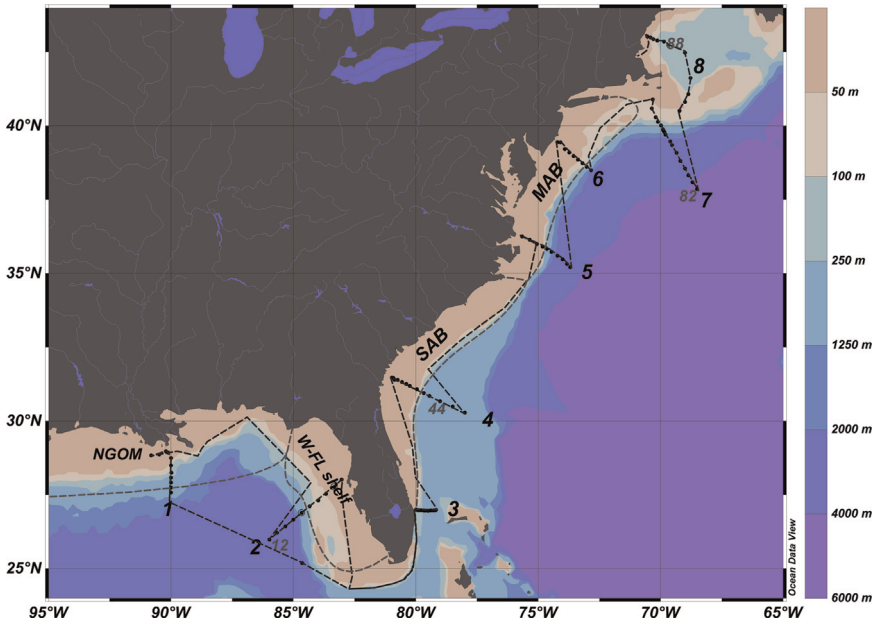

Fig. 1. Map of the study area. The cruise track for the GOMECC-2 cruise is the black dashed line and CTD station locations are the black circles. The gray numbers are the station numbers described in Fig. 2. The bathymetry is a color scale with the legend at the right. The areas of the Northern Gulf of Mexico (NGOM), West Florida Shelf (W-FL shelf), South Atlantic Bight (SAB) and Mid Atlantic Bight (MAB) are delineated by the dashed gray lines. The black numbers identify the different transects: (1) Louisiana, LA line, (2) Tampa line, (3) 27°N line, (4) Georgia, GA line, (5) Cape Hatteras line, (6) New Jersey, NJ line, (7) Line W, and (8) New Hampshire, NH line. (For interpretation of the references to color in this figure legend, the reader is referred to the web version of this article.)

while farther north the 200 m isobath is used. Differences in Ω_{Ar} between the summer cruises in 2007 and 2012 are discussed in the context of anthropogenic CO_2 increases in the coastal waters and natural variability.

The methods section describes sampling, analysis, calculation of saturation state and uncertainty of parameters used in the analyses. The results and discussion section evaluates how Ca^{2+}, CO_3^{2-}, and $K'_{Ar\ sp}$ input parameters impact the calculated Ω_{Ar}. The large-scale surface patterns of relevant parameters affecting Ω_{Ar} are described in terms of inorganic carbon system parameters and nutrients using relevant endmembers. The observed variations, including subsurface patterns, are placed in physical context. Following the descriptions of patterns and processes observed during GOMECC-2, a comparison is made with the summer of 2007 GOMECC-1 cruise. Differences in surface pCO_2, sea surface temperature (SST) and sea surface salinity (SSS) are described followed by observed surface and subsurface changes of Ω_{Ar} and attribution based on large-scale changes in boundary and coastal currents.

2. Methods

2.1. Sampling

Underway samples were taken along the entire cruise track from the scientific seawater supply line, with an intake 5-m below the water line at the bow of the ship. To eliminate potential artifacts from bacterial respiration of organic material in the pipes, the sampling line was flushed thoroughly with bleach and freshwater prior to the cruise (Juranek et al., 2010).

Full water column measurements were performed with a CTD/Rosette system containing 24 10-l Niskin-type bottles. The bottles were subsampled on deck for biogeochemical parameters including DIC, TAlk, $pH_T(25)$, $pCO_2(20)$, O_2, silicate, phosphate and nitrate. Details on all parameters sampled can be found in a comprehensive cruise report (Wanninkhof et al., 2014).

Here, the description is limited to the parameters used in the analysis. Automated systems were used to sample the surface seawater line for fugacity of carbon dioxide (underway pCO_2), SST and SSS at a frequency of 3-min. While the thermosalinograph (TSG) near the bow intake was used for SST, the conductivity cell in the TSG malfunctioned during the cruise such that a TSG unit next to the underway pCO_2 system in the hydrolab was used for salinities. The underway pCO_2 system and its performance characteristics are described in Pierrot et al. (2009). Discrete underway samples for DIC, TAlk, $pH_T(25)$, $pCO_2(20)$, O_2, silicate, phosphate, and nitrate were taken from the scientific seawater supply line at 3-h intervals. Estimated precisions and accuracies are provided in Table 1.

A hull-mounted 75 kHz ADCP was used to determine water velocities, and data were reduced using CODAS 3 software protocols and standards (Firing and Hummon, 2010). The data were averaged to 5-min intervals and depth bins of 4 m. The "surface" bin was at 20–24 m depth due to the draft of the ship and instrument blanking. The ADCP data were primarily used to determine the position of the Gulf Stream, Loop Current and other large-scale oceanographic features.

The CTD was equipped with dual T, S, and O_2 sensors that were compared to assess stability and precision of sensors over time. The sensors were post-calibrated after the cruise and final data were provided using the post-calibrated values from the primary sensor. Differences between the primary and secondary sensors were used to assess the accuracy. They were 0.002 °C in temperature and 0.001 S/m in conductivity. The high accuracy of hydrographic measurements (T, S, and P) was such that their imprecision did not impact the interpretation of the biogeochemical parameters and the calculated values that utilize this information. The salinities and O_2 values from the CTD sensors were adjusted using the shipboard measurements of salinities and O_2 from Niskin bottle samples following the correction routines outlined in the cruise report (Wanninkhof et al., 2014).

Table 1
Accuracy and precision of chemical and physical measurements during GOMECC-2.

Parameter	Method	Vertical resolution (dbar)	Precision	Accuracy
SST (°C)	Thermistor seachest		0.001	0.02
SSS	TSG		0.01	0.02
UWpCO_2 (μatm)	Infrared		0.2	2
T (°C)	CTD probe	1	0.001	0.002
S	CTD probe	1	0.002	0.003
O_2 (μmol kg^{-1})	CTD probe	1	2	3
O_2 (μmol kg^{-1})	Winkler	10–200	1	1.5
DIC (μmol kg^{-1})	Coulometry	10–200	2	2
TAlk (μmol kg^{-1})	Open cell titration	10–200	2	3
pCO_2 (20)[a] (μatm)	Infrared	10–200	0.2%	1%
pH_T (25)[b]	Spectrophotometric	10–200	0.0004	0.001
NO_3 (μmol kg^{-1})	Colorimetric	10–200	0.1	0.2
PO_4 (μmol kg^{-1})	Colorimetric	10–200	0.01	0.02
SiO_4 (μmol kg^{-1})	Colorimetric	10–200	0.1	0.3

[a] Fugacity of CO_2 at 20.00 °C. All pCO_2 values reported throughout are corrected for the non-ideality of CO_2 in air mixtures.
[b] The pH on the total scale at 25.00 °C.

2.2. Chemical analyses

The sampling and analysis protocols for discrete samples closely follow the exacting requirements of the CLIVAR/CO2 repeat hydrography, ocean acidification, and GO-SHIP programs (Dickson et al., 2007; Hood et al., 2010; Dickson, 2010a). DIC was sampled in 300 mL borosilicate bottles and analyzed onboard using a coulometer with an automated sample delivery and gas extraction system using aliquots of about 25 ml. The system was calibrated each time the coulometer cell solution was changed (about every 12 h) by injecting two gas loops of pure CO_2 bracketing the sample concentrations. TAlk was measured by open cell Gran titration of a 25-ml volume of seawater, with daily calibrations of the pH electrode at 3 pH levels (≈ 4, 7, and 10) (Cai et al., 2010). The DIC and TAlk samples were referenced twice a day against certified reference materials (CRMs) (Dickson, 2010b). The pH was measured at 25 °C and reported on the total scale, $pH_T(25)$. The measurements were performed using 10-cm pathlength cuvettes, purified m-cresol purple dye (Liu et al., 2011) and an Agilent 8453 spectrophotometer (Clayton and Byrne, 1993). Samples (500-ml) were measured for discrete pCO_2 with an IR based system similar to that described in Wanninkhof and Thoning (1993), but using a permeable membrane extractor rather than a bubble-type equilibrator. All samples were analyzed within 0.04 °C of 20.00 °C and corrected to 20.00 °C ($pCO_2(20)$) using the empirical correction $d pCO_2/dT = 4.23\%\ °C^{-1}$ (Takahashi et al., 1993). The IR system was calibrated every 3-h using six traceable compressed gas standards with CO_2 concentrations ranging from 248 to 1533 ppm (parts per million by volume).

Carbonate ion concentrations [CO_3^{2-}] were calculated from DIC and $pCO_2(20)$. The [CO_3^{2-}] was also measured using a rapid spectrophotometric technique (Patsavas et al., 2015) but the calculated values showed better precision and provide internal consistency with other parameters such as Ω_{Ar} calculated from the CO2SYS program (Pierrot et al., 2006).

Silicate, phosphate and nitrate were sampled in 30-ml acid-

cleaned plastic bottles and measured with a gas-segmented continuous flow autoanalyzer. Samples were analyzed onboard the ship following the procedure outlined in the GO-SHIP Repeat Hydrography Manual for nutrient measurements (Hydes et al., 2010). Method details and reagent recipes used on this cruise are those routinely used by the AOML nutrient lab (Zhang and Berberian, 1997, Zhang et al., 2000, 2001). Stock standard solutions were prepared with high purity dried solids (KNO_3, KH_2PO_4, and Na_2SiF_6) and the working standards were prepared in low nutrient seawater and referenced against the nutrient CRMs provided by the Meteorological Research Institute of Japan.

Oxygen determinations were performed by Winkler titration. Upon filling the flasks directly from the Niskin, an aliquot of manganous chloride solution was added, followed by the addition of an alkaline sodium hydroxide–sodium iodide solution. The resulting reaction of manganous hydroxide with dissolved oxygen in the water forms a hydrated tetravalent oxide of manganese, and the iodine that is released in stoichiometric proportions is then titrated with sodium thiosulfate. Analysis was performed using an amperometric endpoint detection method following the procedures in Langdon (2010).

2.3. Aragonite saturation state

The aragonite saturation state, Ω_{Ar} is defined in Eq. (2). In the Ω_{Ar} calculations for seawater, $[Ca^{2+}]$ is assumed to be conservative and directly related to salinity: $[Ca^{2+}] = 293.86\ S$ where $[Ca^{2+}]$ is expressed in μmol kg^{-1} (Millero, 1995). $[Ca^{2+}]$ is 50–100 times higher than $[CO_3^{2-}]$. Accuracy of the $[CO_3^{2-}]$ estimate depends on the accuracy of the input parameters (Table 1) and the carbonate dissociation constants. The $K'_{Ar\ sp}$ is expressed in terms of *in situ* temperature, pressure, and salinity using the equations of Mucci (1983). For surface waters (ambient pressure):

$$pK'_{Ar\ sp0} = -\left(-171.945 - 0.077993\,T + 2903.293/T + 71.595\log(T) + (-0.068393 + 0.0017276\,T + 88.135/T)S^{0.5} - 0.10018\,S + 0.0059415S^{1.5}\right) \quad (3)$$

where $pK'_{Ar\ sp_0} = -\log K'_{Ar\ sp_0}$, T is temperature in Kelvin (K), and S is salinity. The pressure dependence is formulated in terms of the change in molal volume and compressibility as described in Millero (1995) using the corrected constants as presented in Appendix A.11 of Zeebe and Wolf-Gladrow (2001):

$$pK'_{Ar\ spP} = pK'_{Ar\ sp0} - 0.434(-((-46 + 0.5304(T - 273.15))/RT(P/10))) + (0.5(-0.011760 + 0.003692(T - 273.15))/RT(P/10)^2) \quad (4)$$

where the subscripts 0 and P on the solubility products denote conditions at the surface and at pressure P (dbar). The equations for molal volume and compressibility changes with pressure have been converted from the expressions in Zeebe and Wolf-Gladrow (2001) to a log base 10 scale, and all temperatures in Eq. (4) are in K. The original equations are expressed on a natural log scale and °C. The ideal gas constant, R, is 83.13 cm^3 bar $(mol\ K)^{-1}$.

Each mineral phase, such as aragonite, calcite, and metastable forms of calcium carbonate, has a characteristic solubility product, K_{sp}. For a given seawater, the mineral's saturation state, Ω is defined such that values less than one mean that the mineral phase is thermodynamically unstable and has a tendency to dissolve while for values greater than one there will be a tendency to precipitate. In temperate surface seawater, Ω_{Ar} values range from 2 to 5 but there is no evidence of precipitation in open waters. This is attributed to kinetic factors inhibiting crystal formation (Berner et al., 1978). A saturation state of 1 is a biogeochemical threshold and waters with levels below this are termed corrosive.

Table 2
Difference in calculated[a] aragonite saturation states (Ω_{Ar}) using different input parameters.

Combination[b]	Average difference	Std. deviation	#Samples
Ω_{Ar}(pH, pCO_2)–Ω_{Ar}(DIC, pCO_2)	0.02	0.04	1041
Ω_{Ar}(pH, pCO_2)–Ω_{Ar}(DIC, TAlk)	0.007	0.08	931

[a] Salinity and temperature dependence of carbonic acid dissociation constants as fit by Lueker et al. (2000) and $K'_{Ar\ sp}$ from Eqs. (3) and (4).
[b] The parameters in parentheses are the input parameters for Ω_{Ar} calculations using the CO2SYS program. For example, Ω_{Ar}(pH, pCO_2) is the aragonite saturation state calculated from $pH_T(25)$ and $pCO_2(20)$.

Values of Ω_{Ar} were calculated using the CO2SYS program coded in Excel (Pierrot et al., 2006). Since all four inorganic carbon system parameters were measured at high accuracy on GOMECC-2, several different combinations of parameters can be used to calculate Ω_{Ar}. No appreciable differences in the determination of Ω_{Ar} were observed from either the combination of $pCO_2(20)$ and $pH_T(25)$; DIC and $pCO_2(20)$; or DIC and $pH_T(25)$. The determination of Ω_{Ar} from DIC and TAlk showed twice as much scatter as other parameter combinations (Table 2). The highest precision for the Ω_{Ar} and the calculated $[CO_3^{2-}]$ can be obtained from the combination of DIC or TAlk combined with either $pH_T(25)$ or $pCO_2(20)$ (M. Patsavas, personal communication). The combination of $pH_T(25)$ and $pCO_2(20)$ yields excellent precision in $[CO_3^{2-}]$ as well, but this combination is not well suited to calculate TAlk or DIC. Besides differences in precision, each combination shows characteristic biases in Ω_{Ar} (Table 2). Here we use DIC and $pCO_2(20)$ to determine $[CO_3^{2-}]$ and Ω_{Ar} as they were measured by similar methods and high precision on both the GOMECC-1 and GOMECC-2 cruises. The interpretations focusing on large-scale changes are not unduly influenced by the combination used to calculate Ω_{Ar}. In general, both $[CO_3^{2-}]$ and Ω_{Ar} will decrease as the TAlk/DIC ratio decreases.

3. Results and discussion

3.1. Parameters for determining Ω_{Ar}

To place the spatial and temporal trends of Ω_{Ar} in geochemical context, the parameters determining the magnitude of Ω_{Ar}, as defined in Eq. (2) are discussed. For calculations of Ω_{Ar}, concentrations of calcium and carbonate ions need to be determined as well as solubility products. The ranges for each parameter for GOMECC-2 are shown in Fig. 2. Four profiles are highlighted, one in deep water in the GOM (Station 12), one in deep water along line W (Station 82), a profile with high Ω_{Ar} in slope waters of the South Atlantic Bight (SAB) (Station 44), and a shallow profile with low Ω_{Ar} in the Gulf of Maine (Station 88).

Fig. 2a shows in situ $[CO_3^{2-}]$ values for the upper 2000 m calculated for GOMECC-2, with a spread of 80–250 μmol kg^{-1} in surface water and narrowing to a range of 90–100 μmol kg^{-1} below 1500 m. Profiles in deep water in the Gulf of Mexico (GOM) and in the Northeast are similar below 1500 m. Minimum $[CO_3^{2-}]$ values of ≈ 80 μmol kg^{-1} are observed at intermediate depths (500–1200 m) of the GOM associated with waters that can be traced to Antarctic Intermediate water (AAIW). Surface waters with lowest $[CO_3^{2-}]$ for the survey are found in the Gulf of Maine. Subsurface waters with the highest $[CO_3^{2-}]$ are seen in slope waters in the 200–600 m range along the SAB and Mid Atlantic Bight (MAB).

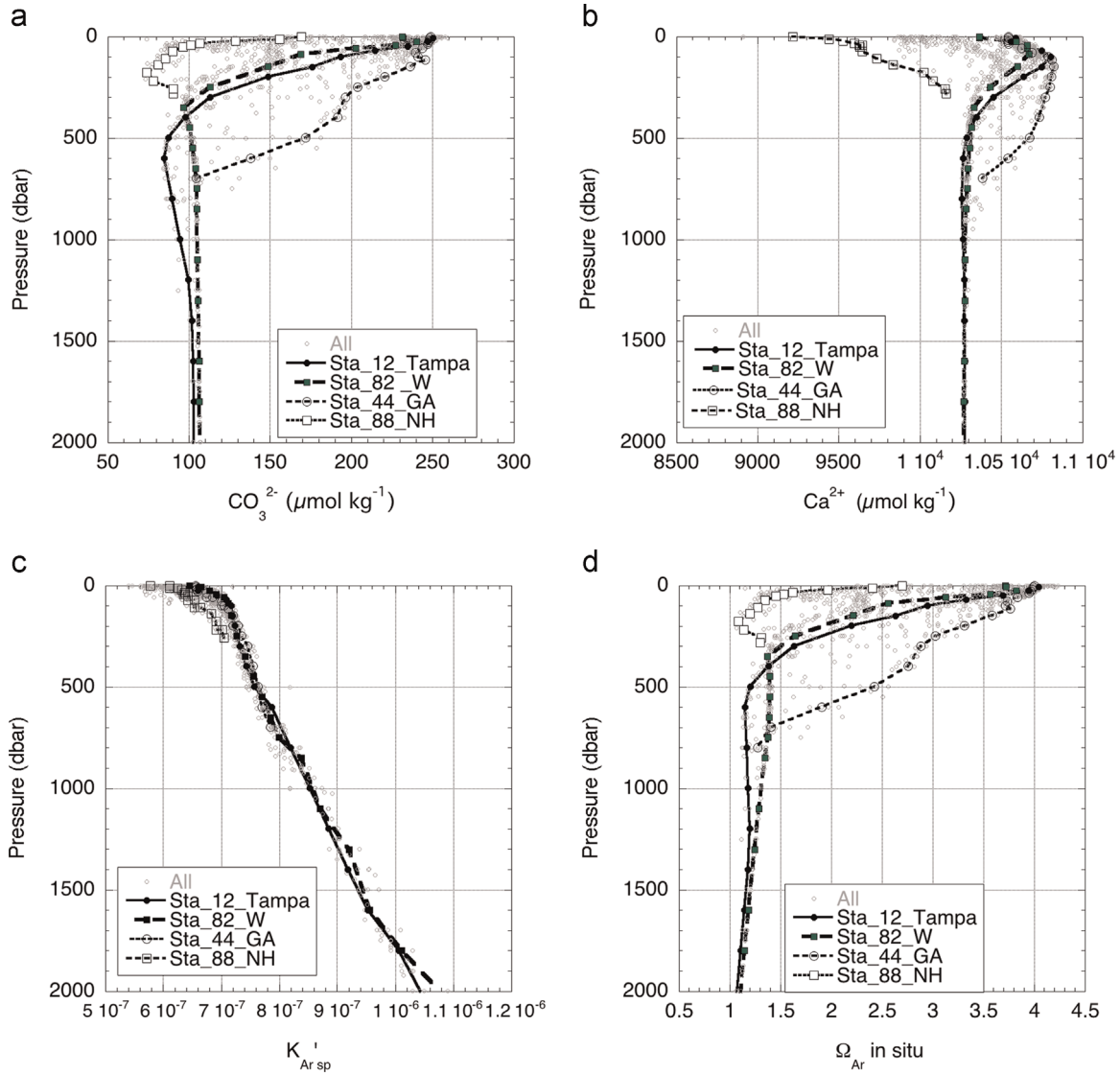

Fig. 2. Parameters used to determine Ω_{Ar} in the upper 2000 m for GOMECC-2. Gray open circles are all the data; the symbols and lines are for the specific stations listed in the insert with locations shown in Fig. 1, $[CO_3^{2-}]$ versus depth (a); $[Ca^{2+}]$ versus depth (b); solubility product $K'_{Ar\ spP}$ versus depth at the *T*, *S*, and *P* (=Pressure) of the samples (c). Aragonite saturation state Ω_{Ar} versus depth at the *T*, *S*, and *P* of the samples (d).

Calcium concentrations $[Ca^{2+}]$ are derived from its proportionality with salinity (Fig. 2b). While there is a 3-fold range in $[CO_3^{2-}]$, the spread in $[Ca^{2+}]$ is only $\pm 10\%$ and therefore less of a determinant for variations in Ω_{Ar}. Samples were taken during GOMECC-2 for Ca^{2+} analysis but have not yet been analyzed. Since many of the rivers in the realm contain appreciable Ca^{2+}, the net effect of the assumed zero intercept of the Ca^{2+} to S relationship will lead to a slight underestimate in the saturation state for low salinity waters influenced by river and groundwater inputs. Low salinity estuarine waters showing variations in $[Ca^{2+}]$ not tied to salinity could affect Ω_{Ar} in areas influenced by these realms.

Eqs. (3) and (4) indicate that $K'_{Ar\ spP}$ increases with increasing pressure and salinity, and decreases with increasing temperature. $K'_{Ar\ spP}$ decreases 10% over the temperature range from 0 to 30 °C. The salinity effect results in a 4% increase in $K'_{Ar\ sp}$ per unit salinity change. The pressure effect on solubility effectively doubles $K'_{Ar\ spP}$ between the surface and the bottom of the ocean (6000 dbar). Pressure effects are most noticeable in deep water since salinity and temperature do not vary appreciably below 2000 m. The profiles of $K'_{Ar\ spP}$ (Fig. 2c) show an increase in the top 200 m mainly due to salinity increases. The more gradual increase between 200 and 2000 m is dominated by an increase in pressure. The effect of pressure on $K'_{Ar\ spP}$ is such that, when a parcel of water with fixed $[Ca^{2+}]$ and $[CO_3^{2-}]$ is upwelled to the surface, the decrease in $K'_{Ar\ spP}$ causes the saturation state to increase. As such, Ω_{Ar} is not a conservative property of seawater.

Fig. 2d shows Ω_{Ar} calculated from DIC and $pCO_2(20)$ for in situ conditions. It closely follows the trends of $[CO_3^{2-}]$ (Fig. 2a) with some modulation from $K'_{Ar\ spP}$ (Fig. 2c). All Ω_{Ar} values are greater than 1 in the upper 2000 m. The Ω_{Ar} decrease to values less than 1 at greater depths is primarily due to increasing $K'_{Ar\ spP}$.

3.2. Surface patterns of Ω_{Ar} during GOMECC-2

Surface Ω_{Ar} in the study region is strongly influenced by large-scale oceanographic features and processes. Because the cruise tracks were well offshore, only the largest nearshore features were observed in our dataset. The nearshore is defined as the region directly impacted by continental processes and runoff, in particular the influence of rivers. Important biological and biogeochemical transformations occur in the nearshore realm, including sediment-water interactions that impact the continental

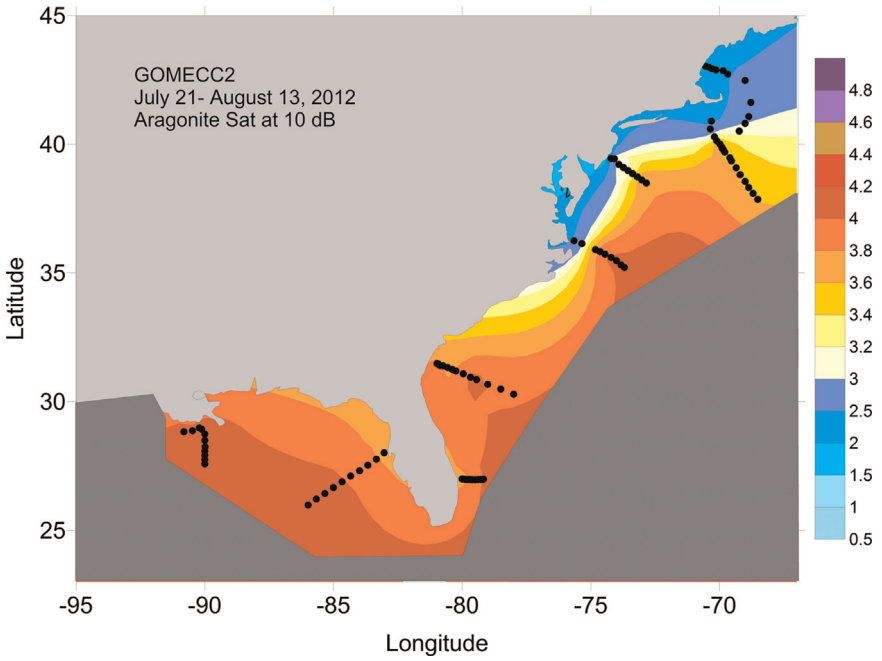

Fig. 3. The Ω_{Ar} on the 10-dbar isosurface. The Ω_{Ar} are accurately represented near the sampling points (black circles) and are interpolated based on an optimal interpolation scheme between locations, DIVA (http://modb.oce.ulg.ac.be/projects/1/diva).

endmembers as inferred from our offshore measurements.

A detailed description of spatial trends of inorganic carbon parameters in the study region can be found in Wang et al. (2013) based on the 2007 GOMECC-1 cruise. The general features in GOMECC-2 are similar to those observed during the 2007 cruise. In short, there is a northward decrease in surface water Ω_{Ar} on the shelf. The observed decrease, from ≈ 4 to ≈ 3 (Fig. 3) is attributed to northward decreases in TAlk and salinity while northward decreases in DIC are smaller than those of TAlk (Fig. 8a, Wang et al., 2013). As such, the TAlk/DIC ratio decreases substantially from south to north. Decreases in both TAlk and DIC correspond to decreases in salinity but the changes do not follow from a simple dilution; rather they are caused by changes in water mass properties. The northern coastal regions are strongly impacted by waters originating from the Labrador Sea and Canadian shelf, whereas those in the south are influenced by mixing between the Gulf Stream and nearshore waters. For Gulfstream waters farther offshore along the shelfbreak, a decrease of approximately 0.5 in Ω_{Ar} is observed between the Florida Current at 27°N 80°W and more northerly Gulf Stream waters at 37°N 68°W. This can largely be explained by a decrease in the TAlk/DIC ratio. Wang et al. (2013) attributed this to entrainment of Sargasso Sea waters into the Gulfstream and perhaps the production of calcium carbonate, although there is no independent corroboration of the latter. Multi-endmember mixing of Gulf Stream waters with coastal inputs and currents from the North could contribute as well.

3.3. Biogeochemical influences

Several investigations, notably Cai et al. (2010), describe trends of salinity and alkalinity in the nearshore region. They attribute many of the nearshore patterns of alkalinity with salinity directly to coastal inputs. Here, trends of Ω_{Ar} and salinity in the surface mixed layer are investigated to determine the impact of coastal inputs on shelf waters, recognizing that Ω_{Ar} is not conservative with respect to mixing and temperature changes. Changes in temperature are not the sole influence on Ω_{Ar} in the region. The 10 °C temperature decrease observed along the coast up to line W would decrease Ω_{Ar} by 0.2 but greater changes are observed.

Fig. 4a shows trends of Ω_{Ar} versus salinity on transects near significant continental (river) outflow including the LA transect impacted by the Mississippi–Atchafalaya river system (MARS), the Cape Hatteras transect influenced by the Chesapeake Bay outflow, the NJ line experiencing the Hudson River outflow and the NH transect that is impacted by the Labrador shelf current. Fig. 4b shows the TAlk–salinity relationship and Fig. 4c shows the DIC–salinity relationship. The TAlk–salinity relationships are robust and suggest near-conservative mixing of a continental endmember with an open ocean endmember. Extrapolation to zero salinity provides an estimate of the alkalinity of coastal inputs, $TAlk_0$. These endmember alkalinities are in general agreement with the endmembers provided in a more detailed analysis by Cai et al. (2010) considering that seasonal variations in $TAlk_0$ of ≈ 200 $\mu mol\ kg^{-1}$ are observed (Guo et al., 2012). $TAlk_0$ and DIC_0 endmembers computed from GOMECC-2 observations are shown in Table 3. As described by Cai et al. (2010), the zero salinity endmembers are not exactly the concentrations of the constituents in the rivers influencing the domain because of biological and geochemical modification in estuaries and nearshore, and multi-endmember mixing of nearby rivers, and coastal and continental effluents. These effects modify $TAlk_0$ and in particular DIC_0 values. The lowest salinities measured on the cruise are around 31 and thus far removed from the actual river inputs such that nearshore processes will affect the extrapolated endmember values. The DIC-salinity relationship (Fig. 4c) shows significantly more scatter than the TAlk–salinity relationship (Fig. 4b) due to the greater impact of biological processes (i.e., respiration and photosynthesis) on DIC than on TAlk. Accordingly, the extrapolation of DIC to zero salinity, and the resulting $(TAlk/DIC)_0$ ratios, should be interpreted with caution. The scatter in DIC is also manifested in the scatter of the Ω_{Ar} versus salinity, indicating how the DIC, and specifically the TAlk/DIC ratio has a first order influence on Ω_{Ar}. The low $(TAlk/DIC)_0$ ratios along the East Coast means that when mixing with shelf waters occurs, coastal inputs will draw down the Ω_{Ar} while, for the MARS outflow with a high $(TAlk/DIC)_0$, increased buffering increases Ω_{Ar}.

The offshore surface patterns of Ω_{Ar} for the region are shown in Fig. 5 in terms of TAlk and DIC with the Ω_{Ar} isopleths

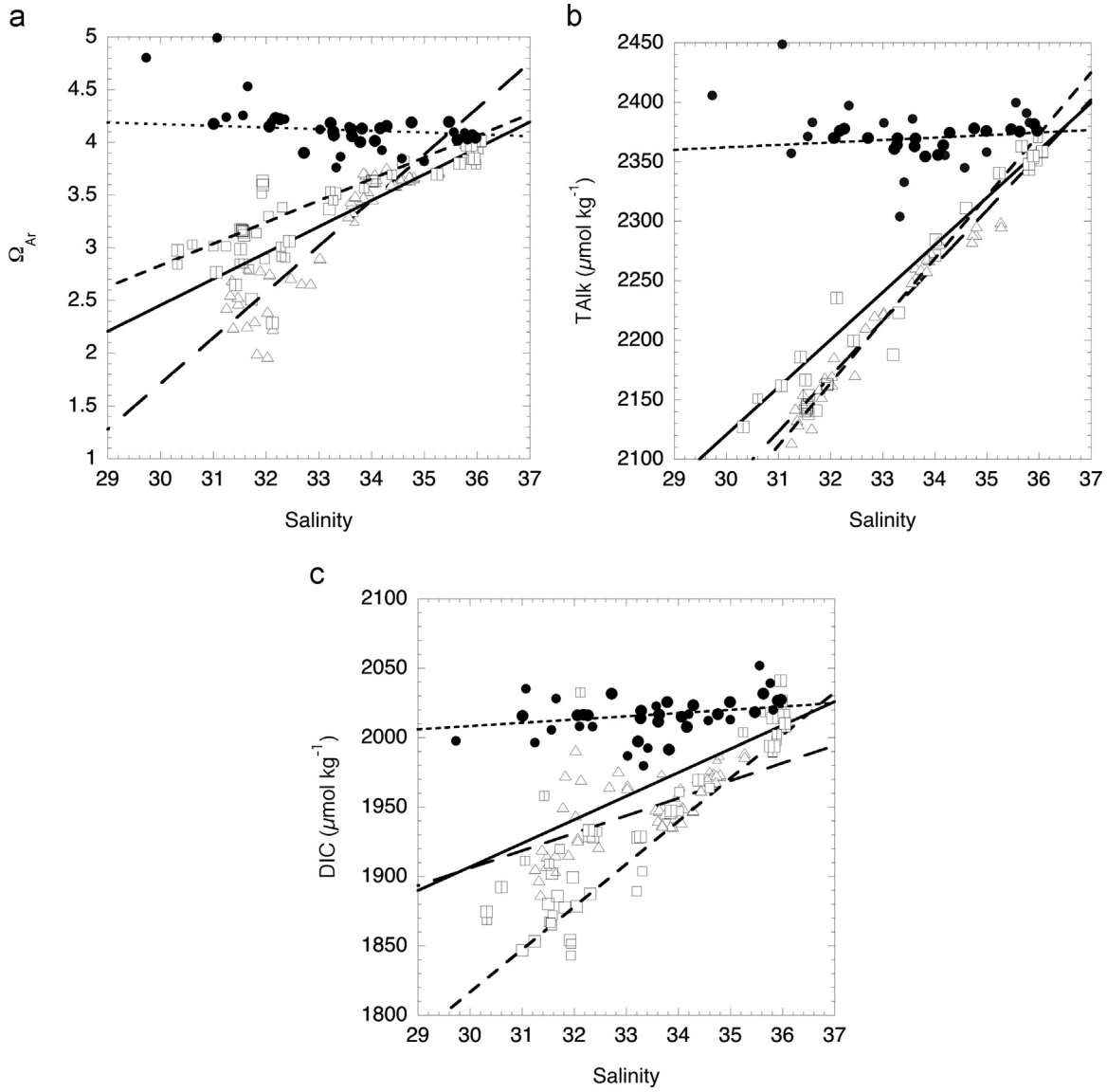

Fig. 4. Relationship of Ω_{Ar} with salinity (a); TAlk with salinity (b); and DIC with salinity (c) in surface water for transects where observations are influenced by riverine outflow. The data include bottle data from the upper 10-m and samples taken from the underway seawater line. The lines are linear regressions through the bottle data to guide the eye. The stippled line is through the LA transect data (solid circles); the dashed line through the Cape Hatteras transect data (open squares); the solid line is through the NJ transect data (squares with vertical line); and the long dashed line is through the NH transect data (triangles).

superimposed. Compared to the continental endmembers, the ranges are smaller. The isopleths follow a TAlk: DIC ratio of 1. Most of the surface Ω_{Ar} values greater than 4 are in the GOM. Samples with Ω_{Ar} between 3 and 4 occur offshore along the East coast. The lowest Ω_{Ar} are found nearshore along the East Coast north of Cape Hatteras, in particular in the Gulf of Maine (also see Fig. 4a). The inset in Fig. 5 depicts an arrow diagram showing the impacts of predominant processes on DIC and TAlk in the absence of coastal inputs. The DIC and TAlk of the GOM samples follow the $\Omega_{Ar}=4$ isopleth, suggesting the predominant effect is evaporation/dilution. The lower Ω_{Ar} (<3) in the Gulf of Maine, and intermediate Ω_{Ar} (3–4) along the Southeast coast, show values spanning a large range of DIC and TAlk with decreasing Ω_{Ar} at lower DIC and TAlk. While this is in accordance with calcification, it is more likely that mixing of northern and southern component waters with different endmembers largely contribute to the observed patterns. Of note, there is no clear signal of photosynthesis in the distribution of data, which suggests that this is not a major contributor in offshore waters and is masked by other processes.

Table 3
Endmember surface values for Ω_{Ar}, TAlk and DIC from linear extrapolation to zero salinity for cross sections impacted by nearshore processes and runoff.

Transect	$TAlk_0$	$TAlk_0$[a]	DIC_0	$(TAlk/DIC)_0$
Louisiana	2303 ± 52	2400	1924 ± 67	1.19
Cape Hatteras	891 ± 40	670	1396 ± 126	0.66
New Jersey	492 ± 108	NA	891 ± 173	0.55
New Hampshire	690 ± 58	800–1150	1522 ± 81	0.45

[a] From a comprehensive study of Cai et al. (2010) with more nearshore data.

3.3.1. *Relationship of Ω_{Ar} with oxygen and nutrients*

Oxygen and macronutrients are key indicators of organic matter remineralization that increases DIC and causes a slight depression of TAlk (Brewer et al., 1975), thus decreasing Ω_{Ar}. The remineralization process can be described by the following equations:

$$(CH_2O)_{106}(NH_3)_{16}(H_3PO_4)+106O_2 \rightarrow 106CO_2+16NH_3+H_3PO_4+106H_2O \quad (5)$$

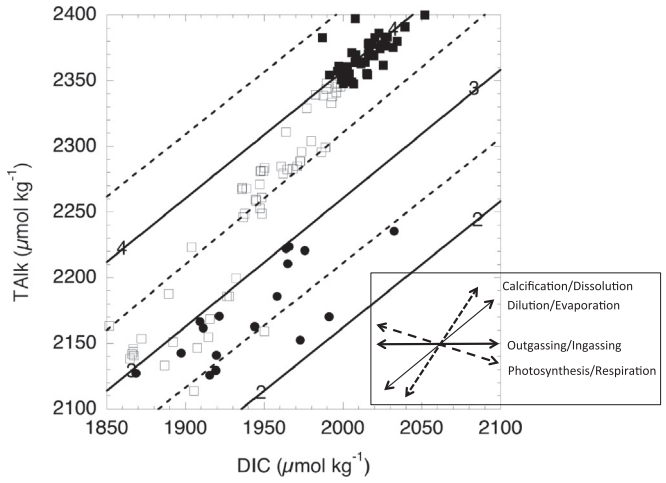

Fig. 5. Surface TAlk plotted against DIC with contours of Ω_{Ar} overlain. The solid squares are samples in the GOM; the open squares are samples offshore of the Southeast coast of the US; while the solid circles are samples on the shelf north of Cape Hatteras. The isolines of Ω_{Ar} are at 0.5 intervals. The arrows in the inset show how TAlk and DIC are impacted by physical and biogeochemical processes with the processes listed in the insert to the right. The first process listed refers to the direction of leftward arrowhead and the second to the rightward arrowhead.

and

$$16NH_3 + 32O_2 \rightarrow 16\ H^+ + 16NO_3^- + 16H_2O \quad (6)$$

where the coefficients are based on a Redfield stoichiometry. The reverse reaction in Eq. (5) is the stoichiometry of aquatic organic material formation by photosynthesis. The changes in Ω_{Ar} during the photosynthesis/remineralization cycles are primarily through CO_2 consumption /production and only secondarily a result of TAlk reduction due to H^+ release (Eq. (6)) and H_3PO_4 production.

The stoichiometric approach to determine processing in the water column is powerful but several caveats should be noted. For shallow water coastal regimes, benthic process can have an influence on the water column and impact the inorganic carbon dynamics. In particular, the anoxic sediments prevalent and possibly expanding in nearshore regimes can influence the alkalinity balance (Hu and Cai, 2011) and change the stoichiometry of DIC production. The Ω_{Ar} in pore waters are often less than 1 with active dissolution. For NO_3, nitrification in surface waters and denitrification in the sediments will impact ratios throughout water column. In particular, Fennel et al. (2006), and Seitzinger and Giblin (1996) suggest large denitrification rates for the MAB. As the GOMECC-2 observations were offshore in water depths greater than 15 m, benthic and nearshore processes do not have determining influence. Wang et al. (2013), Cai et al. (2011) and Jiang et al. (2010), show that signals of continental inputs are largely constrained to the nearshore, except in the MARS system.

On local scales, the impact of remineralization and photosynthesis on Ω_{Ar} can be observed from the vertical patterns of DIC, nutrients and O_2. Higher Ω_{Ar} in the surface layer corresponds to lower DIC and higher O_2 while lower Ω_{Ar} below the mixed layer corresponds to higher DIC, nutrients and lower O_2. On regional scales, relationships between nutrients, O_2 and Ω_{Ar} are heavily influenced by mixing and the endmember characteristics of the water. As part of GOMECC-1, Wang et al. (2013) provide an extensive analysis of carbon dynamics in terms of TAlk and DIC trends as related to salinity and nitrate. Their general results and conclusions hold for the GOMECC-2 effort as well. In broad brush the nutrient and carbon dynamics and their impact on Ω_{Ar} can be explained by a combination of continental inputs, chemical and biological dynamics on the shelf, and offshore endmembers mixing with shelf waters. For the 27°N and GA transects up to Cape Hatteras, the offshore endmembers are the Florida Current and Gulf Stream system that primarily interact with the adjacent shelf water through mixing. For the East Coast transects north of Cape Hatteras, the Labrador Coastal Current defines the endmember. The influence of this coastal current is largely advective as it flows over the shelf.

We build upon these analyses and focus on the trends of Ω_{Ar} with biogeochemical parameters that can be measured autonomously, NO_3, O_2, and pCO_2 (Emerson et al., 2011). For these purposes, pH can be used as well, and the combination of pH and pCO_2 accurately predicts Ω_{Ar} from basic chemical equilibria. NO_3 and O_2 sensors can provide additional information about productivity patterns not available from pH and pCO_2 measurements alone. While remineralization causes changes in NO_3, O_2 and DIC in stoichiometric fashion (i.e., Redfield ratios, e.g. Takahashi et al., 1985), there is no fixed stoichiometry between O_2, NO_3 and Ω_{Ar}. Moreover, the Redfield stoichiometry can break down in the surface layer due to changes in the O_2 and DIC ratio due to air–sea gas exchange. Despite these caveats, Jiang et al. (2010) show for the SAB that trends in NO_3, O_2, and inorganic carbon parameters can be used to qualitatively investigate the impact of productivity on Ω_{Ar}. This analysis is extended to all the cross-shelf transects.

The analysis is performed by determining differences in the mixed layer and immediately below ($\approx$60–80 m). Admittedly qualitative, this simple approach avoids a detailed analysis of a mixing scheme of multiple endmembers that are variable at different transects along the coasts. More importantly, it can provide a first-order assessment of local biological impact on observed subsurface distributions of Ω_{Ar}. The apparent oxygen utilization (AOU) defined as the oxygen concentration at saturation (at in situ S, T) minus the measured oxygen concentrations is used instead of O_2.

To put the differences in the mixed layer and immediately below in context, surface water values are important. In the mixed layer of the offshore oligotrophic southern regions the AOU is about $-5\ \mu mol\ kg^{-1}$, where the minus sign indicates supersaturated conditions, due to heating and bubble dissolution (air injection) in the mixed layer. Supersaturation of up to $-40\ \mu mol\ kg^{-1}$ near the coast is observed in the Northeast. This indicates high productivity as large negative AOU values can only be maintained in situations with large O_2 production. When net productivity diminishes, the AOU will trend to zero due to gas loss through air–sea gas exchange. Nitrate is consistently close to zero and below the detection limit in surface waters, suggesting that the productivity is largely fueled by recycled nutrients in late summer.

In Fig. 6 decreases in Ω_{Ar}, $\Delta\Omega_{Ar}$ between the mixed layer and below (60–80 m depth), are expressed as a % of the surface value to provide a relative magnitude of change. The differences between biogeochemical parameters between the surface and below, ΔNO_3 (Fig. 6a), ΔAOU (Fig. 6b), ΔDIC (Fig. 6c) and $\Delta pCO_2(20)$ (Fig. 6d), all show lower values in the surface compared to below the mixed layer in accordance with remineralization. The Ω_{Ar} is higher at the surface. The scatter for the different parameters varies greatly, with the correlation of $\Delta pCO_2(20)$ and $\Delta\Omega_{Ar}$ being strongest, and ΔNO_3 and $\Delta\Omega_{Ar}$ being weakest. There is an inherent chemical relationship between $pCO_2(20)$ and $[CO_3^{2-}]$, and thus Ω_{Ar}, while NO_3 and Ω_{Ar} are only indirectly related. The correlation between $\Delta\Omega_{Ar}$ and ΔAOU is stronger than that with ΔNO_3, which is attributed to other processes impacting nitrate dynamics such as a greater influence of endmembers and denitrification. NO_3 can denitrify to N_2 and is removed from further biological use on shelves, in particular in bottom waters near the sediments. The smallest NO_3 increases in relation to $\Delta\Omega_{Ar}$ decreases are observed

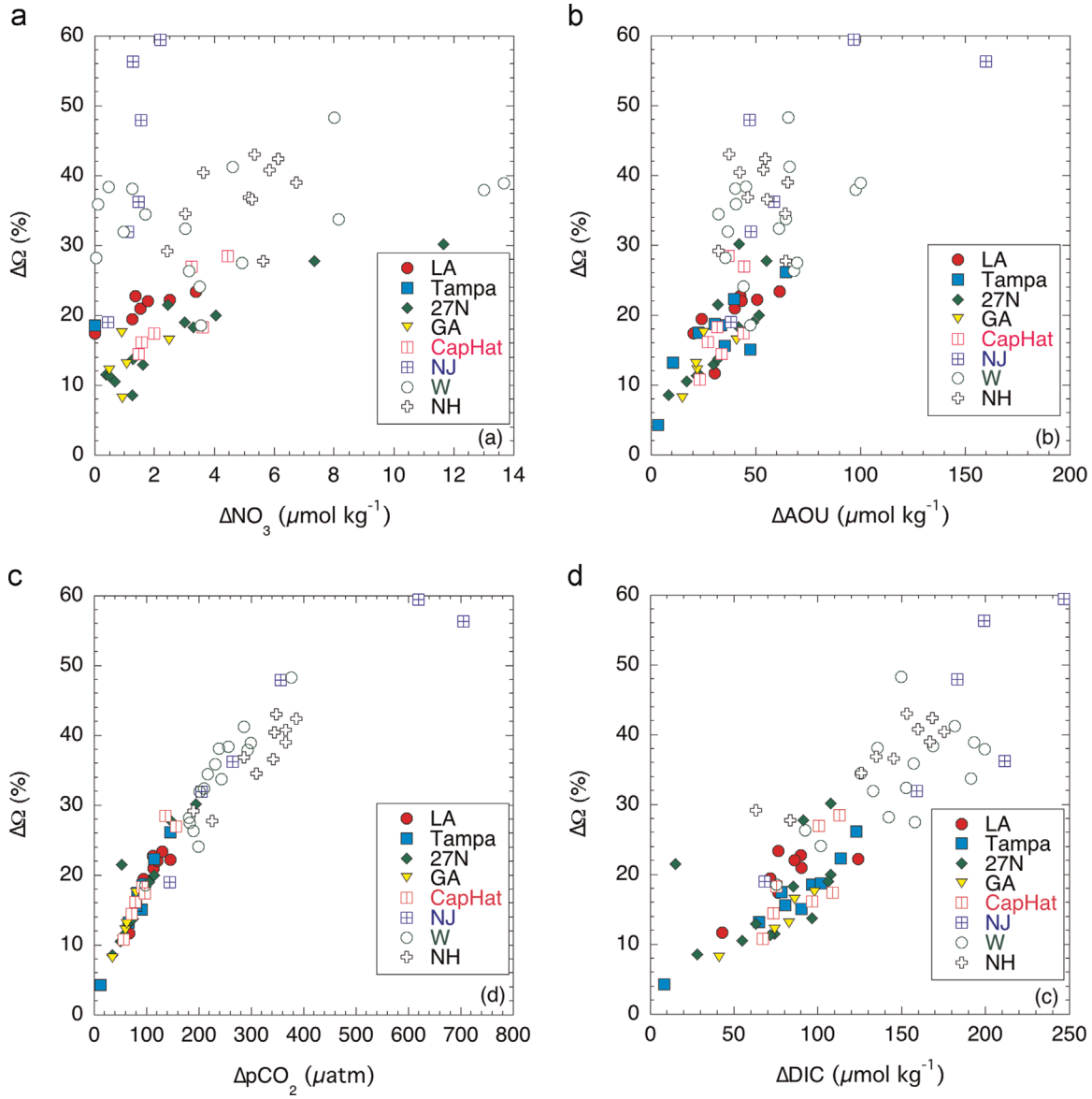

Fig. 6. Differences (Δ) between mixed layer and sub-mixed layer (≈ 60–80 m). The $\Delta\Omega_{Ar}$ are plotted against the increases of chemical properties with depth ΔNO_3 (a): ΔAOU (b); ΔDIC (c); and $\Delta pCO_2(20)$ (d). The $\Delta\Omega_{Ar}$ is expressed as a % decrease relative to the surface Ω_{Ar} value. The symbols in the inserts indicate the different transects shown in Fig. 1.

on the shelves of the MAB (NJ line, Fig. 6a) suggesting a denitrification signal. The stronger correlation between $\Delta pCO_2(20)$ and $\Delta\Omega_{Ar}$, compared to ΔDIC and $\Delta\Omega_{Ar}$ is because increases of TAlk and DIC below the mixed layer have opposite effects on Ω_{Ar} with higher TA increasing Ω_{Ar} and higher DIC decreasing Ω_{Ar}. The $pCO_2(20)$ will increase with increasing DIC and decrease with increasing TAlk and is thus closely inversely related to Ω_{Ar}.

On regional scales observed subsurface variations of biogeochemical parameters are largely controlled by endmembers. Fig. 7 shows patterns of Ω_{Ar} with AOU (Fig. 7a), $pCO_2(20)$ (Fig. 7b) and silicate (Si) (Fig. 7c) for depths greater than 60 m. The prevailing features of the AOU and $pCO_2(20)$ plots versus Ω_{Ar} are curved "mixing lines" with low Ω_{Ar} at high AOU or $pCO_2(20)$. The low endmember Ω_{Ar} values occur at 300–1000 m along the continental slope, and the high Ω_{Ar} endmember is in near-surface waters of the GOM. The appendices are from deep waters (> 1000 m) north of Cape Hatteras, and waters in the GOM at greater than 1500 m depths with salinities slightly less than 35. These deviations are largely caused by the pressure dependence of $K'_{Ar\ spP}$. Fig. 7c shows a Ω_{Ar} versus silicate relationship that is characteristic of parameters impacted by slower remineralization (Rubin and Key, 2002). Within the broad trend, the waters with the lowest Ω_{Ar} and highest silicate values are the deepest waters of the Tampa, Cape Hatteras, and W lines.

3.4. Physical oceanographic influences

3.4.1. Large-scale cross-shelf patterns

The dependencies of Ω_{Ar} on *S*, *T* and inorganic carbon parameters, and their variation with water mass and depth set the large-scale spatial patterns of Ω_{Ar}. Fig. 3 shows the large-scale patterns of Ω_{Ar} at the surface (10 dbar) while the Ω_{Ar} at 100 dbar is presented in Fig. 8. Large-scale patterns at 10 and 100 dbar are coherent and show the strong influence of the endmembers. At the surface and at 100 dbar, waters with low Ω_{Ar} from the North impact coastal Ω_{Ar} down to Cape Hatteras. At the surface the Loop Current and Gulf Stream feature relatively high Ω_{Ar} values and result in high Ω_{Ar} in the GOM and SAB to Cape Hatteras where the

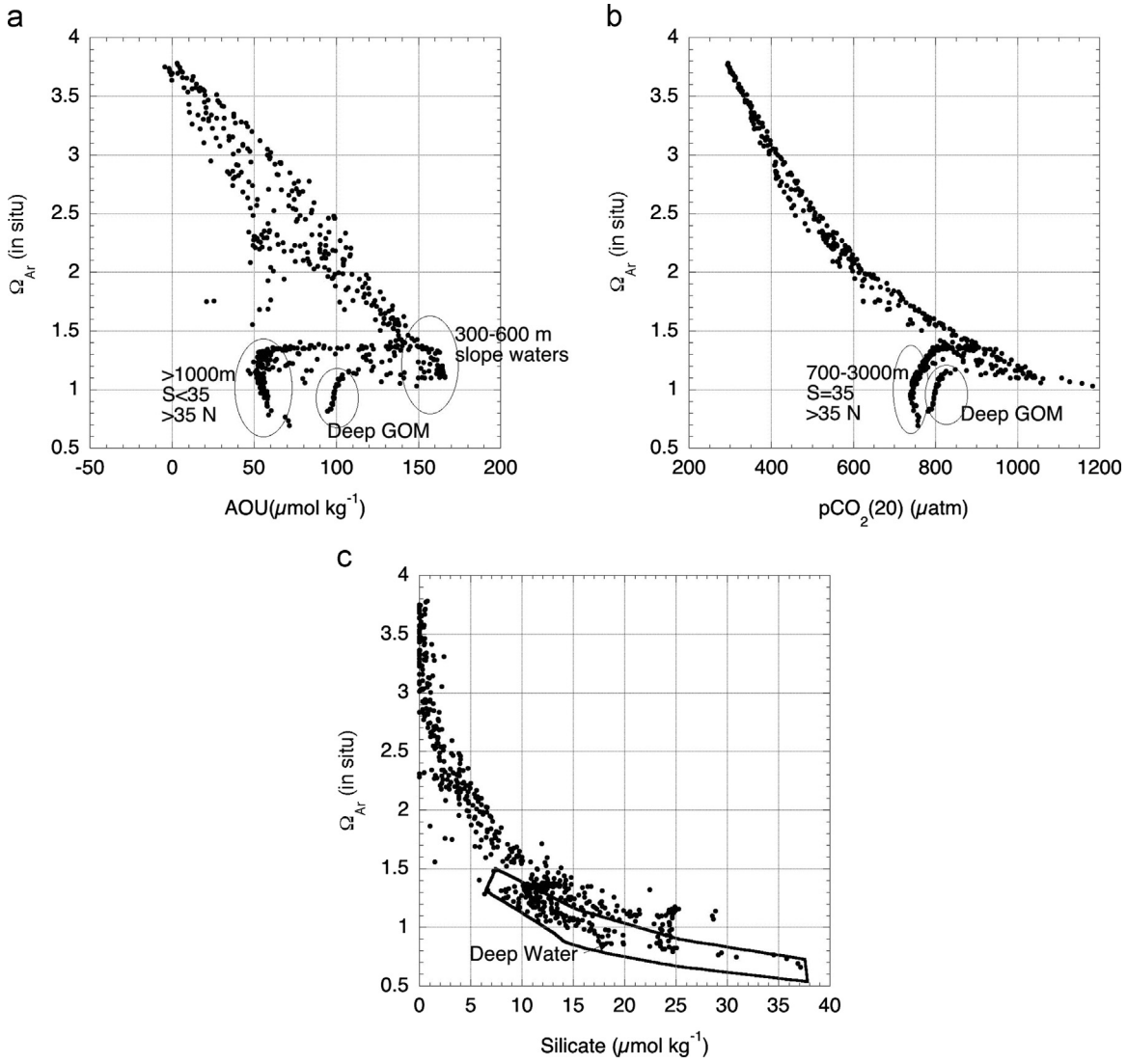

Fig. 7. The AOU (a); $pCO_2(20)$ (b); and silicate (c) plotted against Ω_{Ar} (at in situ T and P) for samples >60 m. Anomalies in the trends are circled in the graphs and discussed in the text.

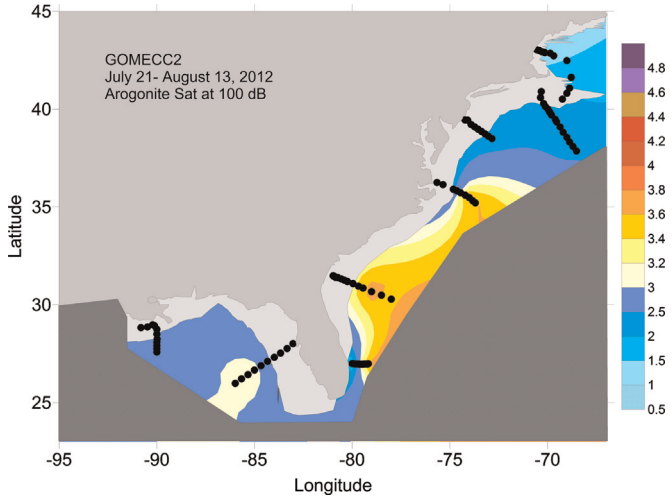

Fig. 8. The aragonite saturation state on the isosurface of 100-dbar. The Ω_{Ar} are accurately represented near the sampling points (black circles) and are interpolated on the pressure surface based on an optimal interpolation scheme.

Gulf Stream separates from the coast. This pattern is reflected at 100 dbar for the Gulfstream but is less clear for the Loop Current due to station locations in the GOM that did not reach the Loop Current in the summer of 2012 (see Appendix A Fig. A3). Of note are the lower Ω_{Ar} values along the shelfbreak at 100 dbar along the Southeast Coast (Fig. 8). These waters contain AAIW and are forced onto the slope through physical dynamics (Atkinson, 1983). They are a source of depressed Ω_{Ar} in an area of otherwise high Ω_{Ar}. While much of the depression of coastal Ω_{Ar} along the East coast occurs through mixing at the bottom of the mixed layer rather than upwelling, coastal storms can cause episodic upwelling and impact local ecosystems by bringing high pCO_2 waters to the surface (Manzello et al., 2013).

Differences between the offshore and nearshore Ω_{Ar} values in the upper 200 m of the water column are shown by cross sections in Fig. 9 arranged in sequence from the LA transect to NH line. The Ω_{Ar} offshore at depth impacts Ω_{Ar} nearshore at shallower depths as can be seen by the shallowing of isopleths of Ω_{Ar}. On large-scale, the nearshore pattern mimics the offshore pattern from the LA to the GA line, indicating the prevailing influence of the open

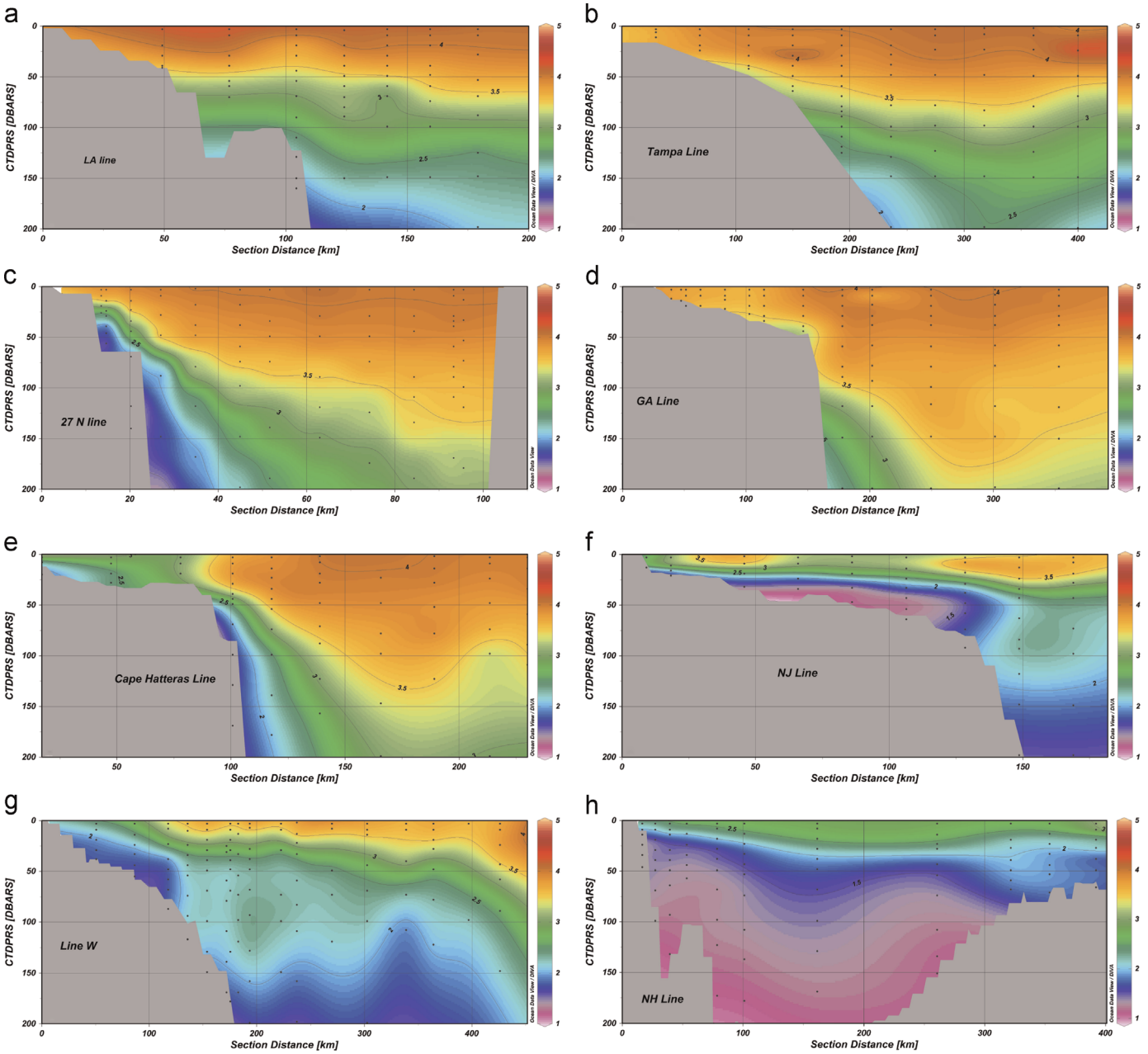

Fig. 9. Cross sections of Ω_{Ar} of the upper 200 m for the transects (Fig. 1) in the sequence they were occupied (a through h). All sections are plotted as nominal distance from the coast (in km) with different length scales. Sampling depths are shown as solid circles. Plots are created in Ocean Data View (Schlitzer, 2014).

ocean on the coastal region. On closer inspection there are discernable differences between the nearshore and offshore. For example, due to the MARS influence, the nearshore surface Ω_{Ar} values near the coast of Louisiana are higher ($\Omega_{Ar} \approx 4.3$) than the corresponding offshore values ($\Omega_{Ar} \approx 4.0$), due to high Ω_{Ar} in the lower salinity waters with high $(TAlk/DIC)_0$. This is due to a combination of high TAlk riverine water and biological drawdown of DIC in the plume (Guo et al., 2012) (Fig. 4, Table 3). Also of note is the low Ω_{Ar} along the western boundary of the Florida Straits (27°N line), showing the impact of AAIW-influenced waters flowing through the straits close to the surface. From Cape Hatteras northward there are appreciable differences between offshore and nearshore due to the southward flowing coastal currents on the shelf. The offshore trends show the waning influence of the Gulfstream, with surface values Ω_{Ar} decreasing to 3. The Ω_{Ar} at 100 m reaches as low as 2 further north. Nearshore surface Ω_A values show a similar decrease but with values that are ≈ 0.5 less than the corresponding values offshore. For the Cape Hatteras line, fresh water from the Chesapeake Bay contributes to lower nearshore surface Ω_{Ar} values (Fig. 4a).

3.4.2. *The deep Ω_{Ar} minima along the 27°N line and Cape Hatteras and New Jersey sections*

The Ω_{Ar} is less than 1.5 in the central and western section of the 27°N line at depths below 400 dbar (Fig.10a). These waters have AAIW origins and move northward (Atkinson, 1983). The feature gets to within 75 m of the surface on the western edge of the 27°N section. The waters are characterized by low temperature, low salinity (not shown), high AOU (Fig. 10b), and low alkalinity (Fig. 10c) but have high DIC (Fig. 10d) and silicate. The low Ω_{Ar} water moves along the western edge of the Gulf Stream (see GA and Cape Hatteras lines, Fig. 9) and can enter into the euphotic zone of the SAB shelf due to eddies (Lee et al., 1991). Because of its high DIC to TAlk ratio and therefore low Ω_{Ar}, these waters have an

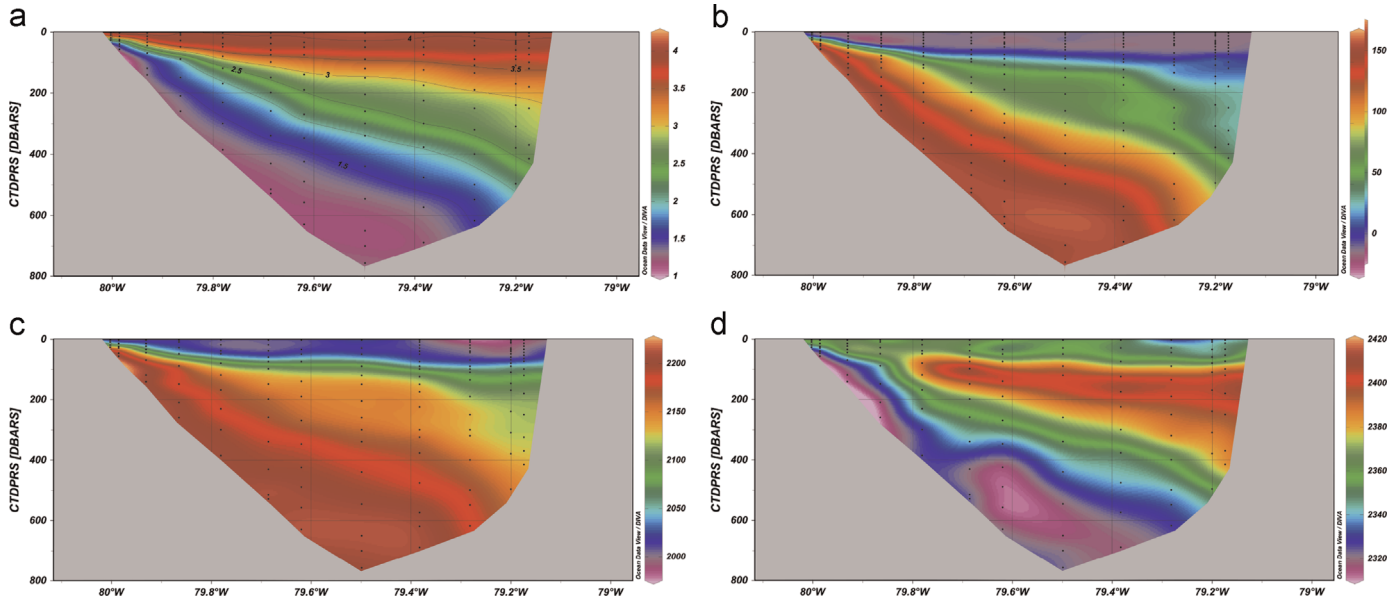

Fig. 10. Contour plots of Ω_{Ar} (a); AOU (b); DIC (c); and alkalinity (d) in the Florida Straits (27°N line). The plots are created in Ocean Data View (Schlitzer, 2014).

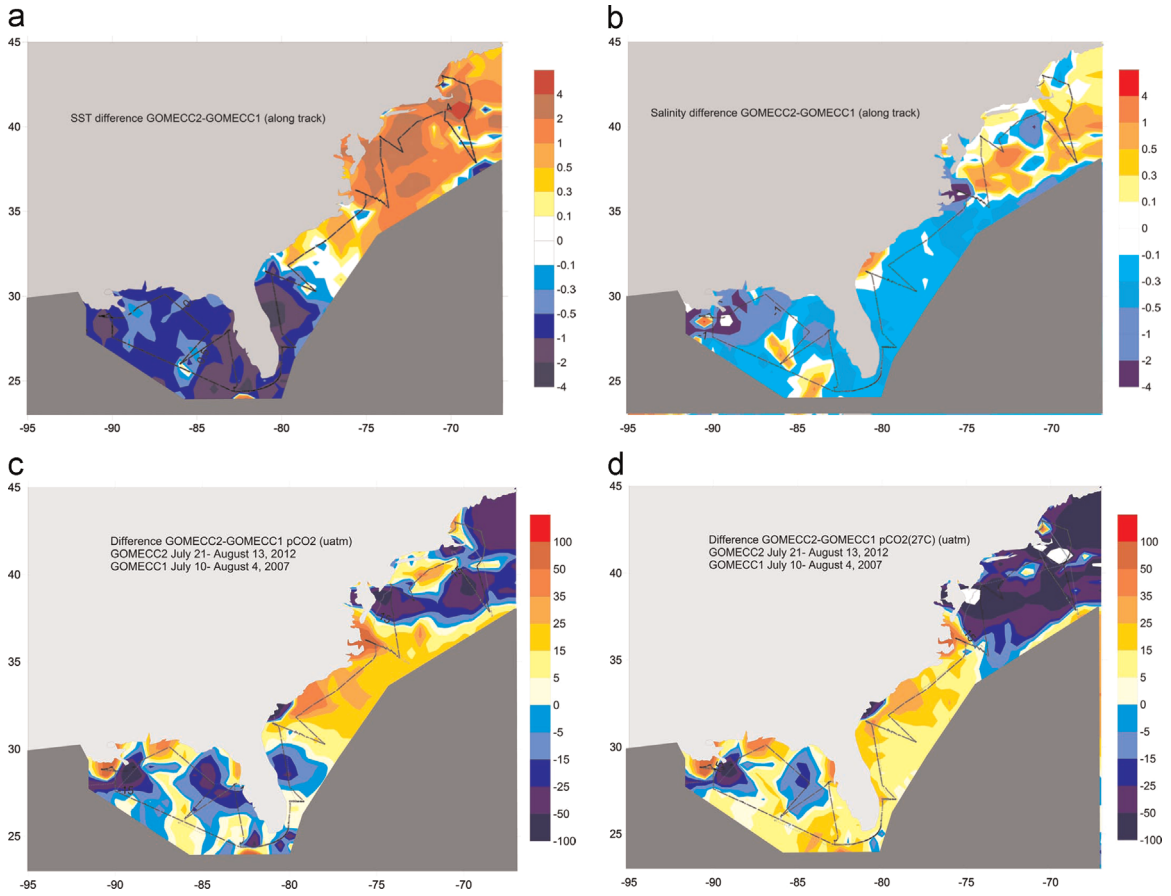

Fig. 11. Differences between GOMECC-2 and GOMECC-1. Data from the underway sea water system along the cruise tracks for the two cruises are extrapolated and bin-averaged in 0.5° grids and subtracted: SST difference (a); salinity difference (b); pCO_2 difference (c); $pCO_2(27)$ difference (d).

appreciable influence on the coastal Ω_{Ar} in this region.

Another key low Ω_{Ar} subsurface feature is observed on the shelf at the edge of the shelfbreak of the Cape Hatteras and NJ lines. The waters originate from the north as a cold water coastal flow (Fig. 9). Moving southward, the DIC in these waters increase due to remineralization, causing lower Ω_{Ar} (Jiang et al., 2010). Exactly how these boundary currents impact the surface values and benthos nearshore is difficult to quantify, but the proximity of these currents with low Ω_{Ar} to the surface, suggests that the influence and variability of these currents on coastal waters is significant. High-resolution physical dynamical models that incorporate biogeochemistry will aid to properly determine the contribution of offshore subsurface Ω_{Ar} minima to nearshore impacts (Hofmann et al., 2011).

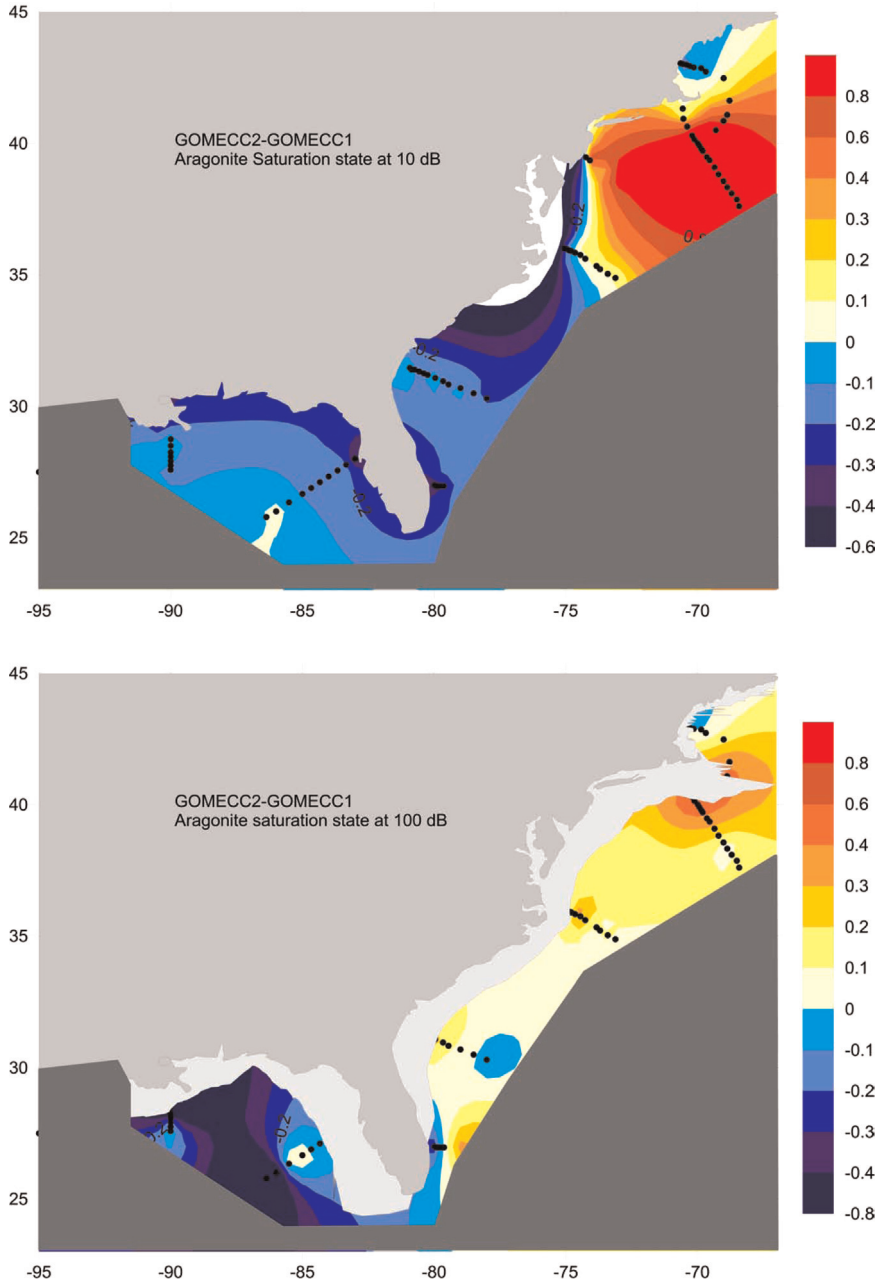

Fig. 12. Differences in Ω_{Ar} along isosurfaces of 10 dbar (a) and 100 dbar (b) between GOMECC-2 and GOMECC-1. Data from the cross-shelf transects are extrapolated, bin-averaged in 0.5° grids and then subtracted. GOMECC-2 stations are shown.

3.5. *Changes between GOMECC-1 in 2007 and GOMECC-2 in 2012*

3.5.1. *Changes in surface water pCO_2, SST and SSS*

The GOMECC-1 cruise in 2007 and GOMECC-2 cruise in 2012 were both performed during the summer season (July/August). Over the 5-year period atmospheric CO_2 levels increased by 10 ppm or 2.5% (from 384 ppm to 394 ppm) based on the Mauna Loa, HI and Key Biscayne, FL marine atmospheric boundary layer time series (Cooperative Global Atmospheric Data Integration Project, 2013). This translates to a 10 μatm increase in surface water pCO_2 levels if the surface ocean tracks the atmosphere, as is the case for most of the global ocean (Takahashi et al., 2009). The change in Ω_{Ar} due to increases of pCO_2 and DIC will depend on the absolute Ω_{Ar} level and the buffer capacity of the water, but is roughly 2% over the time period. Assuming a 10 μatm increase in pCO_2 and using a representative surface water DIC of 1980 μmol kg^{-1}, a TAlk of 2340 μmol kg^{-1}, a SSS of 36 and a SST of 24 °C, this would lead to an Ω_{Ar} change of 0.08. Observations between the two cruises show both large positive and negative changes in Ω_{Ar}, indicating that natural changes rather than anthropogenic inputs dominate in this coastal regime.

The surface maps (Fig. 11) provide a regional representation, but the spatial extent of riverine and nearshore anomalies are likely exaggerated in space due to the gridding approach and the paucity of data in the horizontal. Higher resolution approaches for pCO_2 mapping along the East Coast can be found in Signorini et al. (2013). A qualitative measure of smaller scale variability and differences is gleaned from comparison of high-resolution (1/4°) model output of SST and SSS (Appendix Figs. A1 and A2) with along-track SST and SSS (Fig. 11a and b). While on small scale there are differences, particularly along the Gulfstream, on broader scales there is good correspondence.

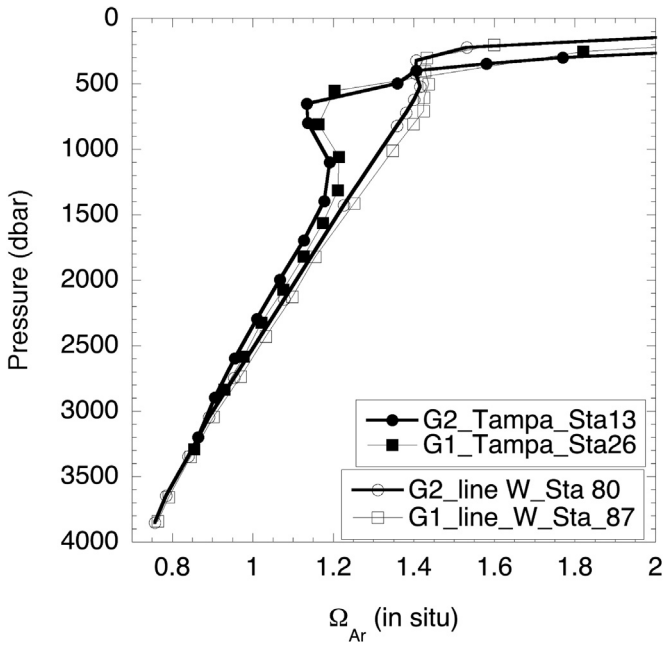

Fig. 13. The Ω_{Ar} (in situ T and P) for deep stations at the end of the Tampa line and line W (see Fig. 1). The solid symbols are for the station on the Tampa line and the open circles for line W, with circles and thick solid line depicting GOMECC-2 (G2) and squares and thin line GOMECC-1 (G1).

Appreciable differences in SST and SSS are observed between the summer of 2012 and 2007, with strong positive correlations between anomalies in SST and SSS (Fig. 11a and b). On large scale, the GOM and the track up to Cape Hatteras show lower SST and SSS in 2012 while, at higher latitudes, SST and SSS predominantly show increases between 2007 and 2012. If we only consider the thermodynamic controls of SST and SSS on the pCO_2, lower SST would decrease the pCO_2 by $\approx 4.23\%\ ^{\circ}C^{-1}$, and lower SSS would decrease the pCO_2 by $\approx 10\ \mu$atm per mil salinity (Takahashi et al., 1993). Thus, after accounting for an increase of 10 μatm in response to increased atmospheric CO_2, surface water pCO_2 is expected to be less in the regions with lower SST and SSS in 2012 compared to 2007 and higher in regions with the opposite trends. Fig. 11c shows that this is not universally the case. As such, water mass changes play a significant role. In the GOM, East Florida shelf and SAB regions there are large areas where the pCO_2 decrease follows the SST and SSS decreases observed in 2012 compared to 2007. However, North of Cape Hatteras where the Gulf Stream departs the coast there is a strong anti-correlation. SST and SSS increase and a pCO_2 decrease over the five-year period between GOMECC-2 and GOMECC-1.

The MAB and large parts of the Gulf of Maine had the highest SST on record for the summer of 2012 driven by air–sea heat flux anomalies during the preceding winter and spring (Chen et al., 2014). The changes in pCO_2 cannot be explained merely by heating. Fig. 11d shows changes in surface water CO_2 levels after accounting for thermodynamic effects (caused by changes in SST and SSS) calculated by normalizing the data of both cruises to SST = 27 °C and SSS = 34.5 using the CO2SYS program (Pierrot et al. 2006). The SST and SSS values of 27 °C and 34.5 used for the normalization are roughly the averages for the 2012 cruise. The figure shows predominant increases of $pCO_2(27)$ in the GOM and along the East Coast, ranging from 5 to 20 μatm, in broad agreement with the 10 μatm increase expected from the rising atmospheric CO_2 levels. The large decreases in $pCO_2(27)$ between cruises further north are closely associated with positive SSS anomalies in 2012 compared to 2007, and are attributed to a smaller contribution of low-salinity, high pCO_2, northern component waters to the coastal ocean in the Northeast.

Changes in the GOM are closely associated with the trajectory of the Loop Current and are described in terms of relative 2012 and 2007 observations. The salinities and temperatures were lower in the MARS outflow region in 2012. These did not correspond with river outflow values that showed 25% lower flows from the MARS system in 2012 compared to 2007 during the spring and summer (based on the St Francisville, MS stream gaging site 07373420). Remotely sensed altimetry, SST and model derived SSS (Appendix A) show a well-developed Loop Current in 2007 that reached the coast just east of the MARS outflow (Fig. A3a). Most of the SSS anomalies associated with the MARS flow extended towards the west in 2007. The salty waters of the loop current are seen all along the West Florida Shelf in 2007. The model flows for 2012 showed a predominantly weak easterly current in the Northern GOM (Fig. A3b). This flow pattern is conducive to entraining the MARS water southeastward along the West Florida shelf (Le Hénaff et al., 2014), contributing to the low SST, SSS and pCO_2 in the region in 2012.

Like the regional differences in SSS and SST, the differences in pCO_2 between the cruises are not systematic, and large differences between the two cruises mask the expected pCO_2 increase of ≈ 10 μatm. In broad brush, nearshore areas in the Northern GOM and most of the East Coast up to and including the Cape Hatteras transect show pCO_2 increases of ≈ 10–30 μatm. For large regions offshore in the GOM and West Florida Shelf, and in the Northeast, the pCO_2 levels in surface waters are significantly less for GOMECC-2 compared to GOMECC-1. As seen by comparing Fig. 11c and d, some of these differences diminish when changes in SST and SSS between the cruises are taken into account, particularly in the Southeast, but thermodynamic influences due to variations in SST and SSS do not explain the observed changes in the GOM and Northeast.

3.5.2. *Surface and subsurface changes in Ω_{Ar}*

Contoured sections of Ω_{Ar} differences between 2007 and 2012 in the subsurface at 10 and 100 dbar are based on the cross-shelf transects at the same locations for both cruises (Fig. 12). For the surface, the underway pCO_2, SSS, and SST measurements are shown (Fig. 11) as these parameters are sensitive indicators of changes in inorganic carbon chemistry and strong predictors of Ω_{Ar}. The large-scale differences between cruises are evident in both the surface and subsurface Ω_{Ar}. For consistency and comparison, surface (10 dbar) and subsurface (100 dbar) Ω_{Ar} data for the two cruises are compared along the 8 transects (Fig. 1) utilizing the isosurface interpolating routines of Ocean Data View (Schlitzer, 2014). They are coarse interpolations in the horizontal but, based on high-resolution SST and SSS (Appendix A Fig A1 and A2) and inspection of observations along the transects, the large features reflect real differences. In the vertical there are negligible interpolation artifacts onto the 10 and 100 dbar surfaces since samples were taken at 10–20 dbar intervals.

The Ω_{Ar} at 10 dbar in the GOM and East Coast up to the MAB, are 0.1 to 0.2 less in GOMECC-2 than GOMECC-1 with decreases up to 0.5 along the Cape Hatteras transect. Further north there is an increase of up to 0.5 in Ω_{Ar} between the two cruises. At 100 dbar the pattern of Ω_{Ar} changes differs from the surface. In the GOM there is a greater decrease in Ω_{Ar} at 100 dbar than at 10 dbar, while in the SAB and MAB there is an increase over the 5-year time span. The changes in Ω_{Ar} can be largely explained in terms of changes in major circulation features and corresponding changes

in T, S and inorganic carbon parameters controlling Ω_{Ar}. In the GOM the Loop Current, with high Ω_{Ar}, was less pronounced during GOMECC-2, causing slope waters with lower Ω_{Ar} to exert a greater influence at the surface and particularly in the subsurface. Along the East Coast the increase in Ω_{Ar} at 100 m shows that the low Ω_{Ar} waters from the north were less prevalent during GOMECC-2, causing an increase along much of the shelf and slope with the greatest increase nearer to the northern origin waters. At the surface, waters from Chesapeake Bay, with low Ω_{Ar}, exerted a greater influence on the shelf in 2012 and caused a large depression in salinity and Ω_{Ar} during GOMECC-2, while at 100 m the Ω_{Ar} is higher for GOMECC-2. Further North the Ω_{Ar} increase over the entire top 100 m and changes are up to 0.6 at 10 dbar compared to 0.2 at 100 dbar, again attributed to decreased northern end-member waters.

The Ω_{Ar} at 10 dbar is generally anti-correlated to the pCO_2 as is expected from the relationship between $[CO_3^{2-}]$ and $[CO_2]$. This is seen along the East Coast where increasing/decreasing pCO_2 (Fig. 11c and d) corresponds to decreasing/increasing Ω_{Ar} (Fig. 12 a). However, in the GOM there are regions where decreases in pCO_2 correspond to decreases in Ω_{Ar}, particularly along the Tampa transect. The decreases in Ω_{Ar} in the GOM at the surface and 100 m also manifest themselves as small but consistent changes in the deepwater Ω_{Ar} down to 2500 dbar as shown in Fig. 13 for deep water stations at the end of the Tampa line and line W. The deep water changes correspond to decreases in TAlk of about 5 μmol kg^{-1} in water between 500 m and 2000 m; small increases in DIC of 1–3 μmol kg^{-1}, and increases of 10–15 μatm in $pCO_2(20)$ in the deep waters of the Tampa line. The T and S was 0.03 °C warmer and 0.003 fresher over this depth range, confirming the existence of a different water composition rather than effects from internal waves or mixing. For Line W, the Ω_{Ar} surface water was greater in 2012 than in 2007. However, the deep Ω_{Ar} values are systematically less between 300 and 1500 m in 2012 (Fig. 13). The deep water also showed a 0.02 decrease in salinity, and 15 μatm higher $pCO_2(20)$ in 2012 compared to 2007. Differences in Ω_{Ar} between the cruises for the two locations converge at depths >3000 m.

4. Conclusions

As it pertains to ocean acidification, aragonite saturation states, Ω_{Ar}, are a good thermodynamic indicator of changes in inorganic carbon chemistry in that they provide a means to determine the impact of increasing seawater CO_2 levels on the stability of the aragonite mineral phase. Many shell-forming organisms are sensitive to the magnitude and change of aragonite saturation state. The Ω_{Ar} is proportional to the $[CO_3^{2-}]$ that can be determined at greatest precision using DIC or TA in combination with either $pCO_2(20)$ or pH(25). The combination of pH(25) and $pCO_2(20)$ provides equal precision and is attractive since both parameters can be determined autonomously. The GOMECC cruises provide a regional view of Ω_{Ar} and changes thereof. High values, with $\Omega_{Ar} \approx 4.5$, occur in the GOM and decrease going northward along the Eastern Seaboard with Ω_{Ar} values reaching 2 in the Gulf of Maine during summer. There are decreases as large as 0.5–1 going towards shore along the East coast that are caused by a combination of riverine outflow, vertical mixing and excess remineralization resulting from nearshore eutrophication. Subsurface values of Ω_{Ar} decrease appreciably below the mixed layer. The largest changes in Ω_{Ar} with depth are observed in the GOM but Ω_{Ar} remains >1. Large changes in Ω_{Ar} are observed between the two summertime occupations in 2007 and 2102. While survey-wide patterns in Ω_{Ar} are similar between cruises there are large regional differences in Ω_{Ar} ranging from -0.5 to 0.5 in surface water. This is 5–10 times greater than expected from anthropogenic CO_2 input from the atmosphere which would lead to a change in Ω_A of 0.05–0.1 in surface water. At 100 m, below the summer mixed layer, changes vary from -0.2 to 0.2. Decreases in Ω_{Ar} of ≈ 0.1 are observed down to a depth of ≈ 2000 m at the end of the Tampa line, and slightly smaller changes are observed offshore at depth along line W. The large differences are primarily attributed to changes in current strength and location. In the Northern GOM and West Florida shelf the influence of the Loop Current with high Ω_{Ar} is less in 2012, and waters with lower Ω_{Ar} prevail in the upper 2000 m. In the Northeast, a decrease in inflow of the Labrador Sea slope water containing low Ω_{Ar} caused an increase in Ω_{Ar} of 0.5 between occupations. Follow-up surveys to document the long-term trends in inorganic carbon dynamics and ocean acidification in these spatially complex and temporally variable coastal environments are necessary. Furthermore, detailed regional studies are needed to improve process level understanding and promote the development of predictive models of ocean acidification in the coastal realm.

5. Data Availability

All measurements from GOMECC-1 and GOMECC-2 can be found at: http://www.aoml.noaa.gov/ocd/gcc/GOMECC1/ and http://www.aoml.noaa.gov/ocd/gcc/GOMECC2/

The GOMECC-2 bottle data and underway pCO_2 data are also available at NODC: http://www.nodc.noaa.gov/oceanacidification/data/0117971.xml

Acknowledgments

We express sincere thanks to participating scientists, captain, officers and the crew of the NOAA ship *Ronald H. Brown* for their assistance in carrying out the GOMECC-2 cruise. Support from the NOAA Ocean Acidification Program (OAP) and the Atlantic Oceanographic and Meteorological Laboratory (AOML), both part of the NOAA Office of Oceanic and Atmospheric Research (OAR) is gratefully acknowledged. Joaquin Trinanes of University of Santiago de Compostela and NOAA Coastwatch provided the remotely sensed and model data in Appendix A.

Appendix A

Sea surface temperature (SST), sea surface salinity (SSS) from remote sensing and modeling.

For surface waters there are several products that aid in determining if the observations from the GOMECC-2 cruise are representative by providing information about spatial heterogeneity. Sea surface temperature (SST) can be obtained at high resolution from a variety of satellites and optimally gridded products. Sea surface salinities near the coast are model-derived based on the Atlantic operational Real Time Ocean Forecasting System (Atlantic RTOFS). The model is a basin-scale ocean forecast system using the HYbrid Coordinate Ocean Model (HYCOM) (Mehra and Rivin, 2010). For consistency the SST is obtained from the same model, which shows excellent agreement with the optimally interpolated SST product (OISST) (http://www.ncdc.noaa.gov/sst/; Reynolds et al., 2007).

Fig. A1 shows the 2-week average SST for July 15–30, 2007 and

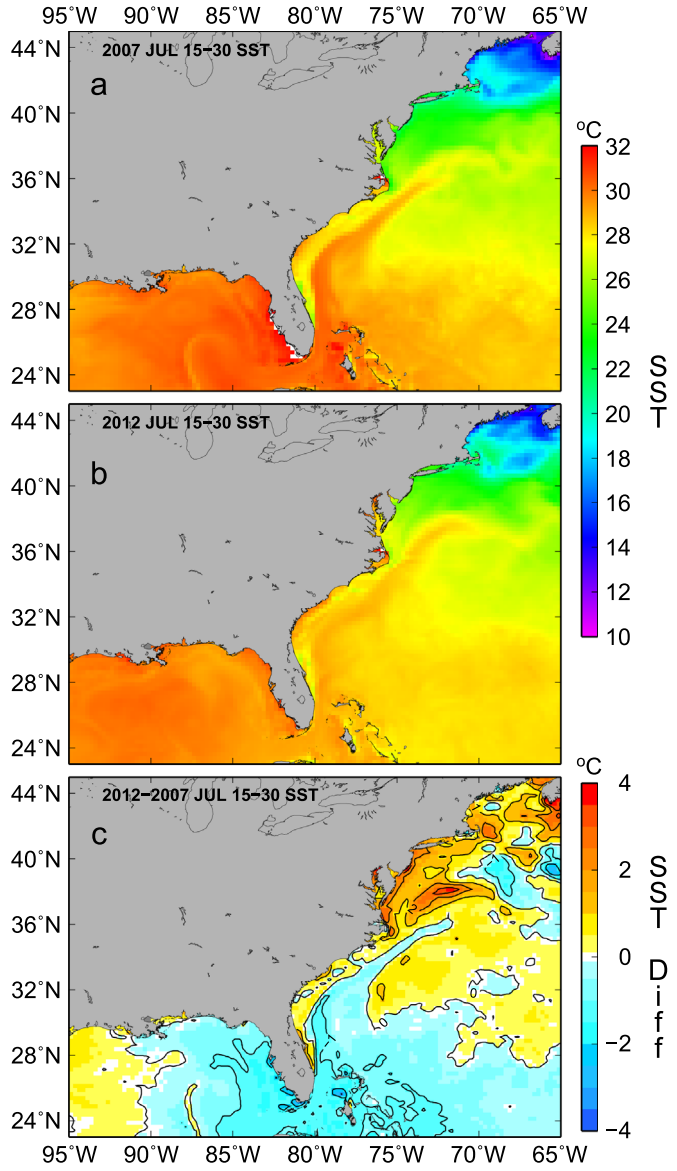

Fig. A1. SST from RTOFS for 2007 (a), 2012 (b) and difference between 2012 and 2007 (c). The bottom panel can be compared with the differences along the cruise track shown in Fig. 11a.

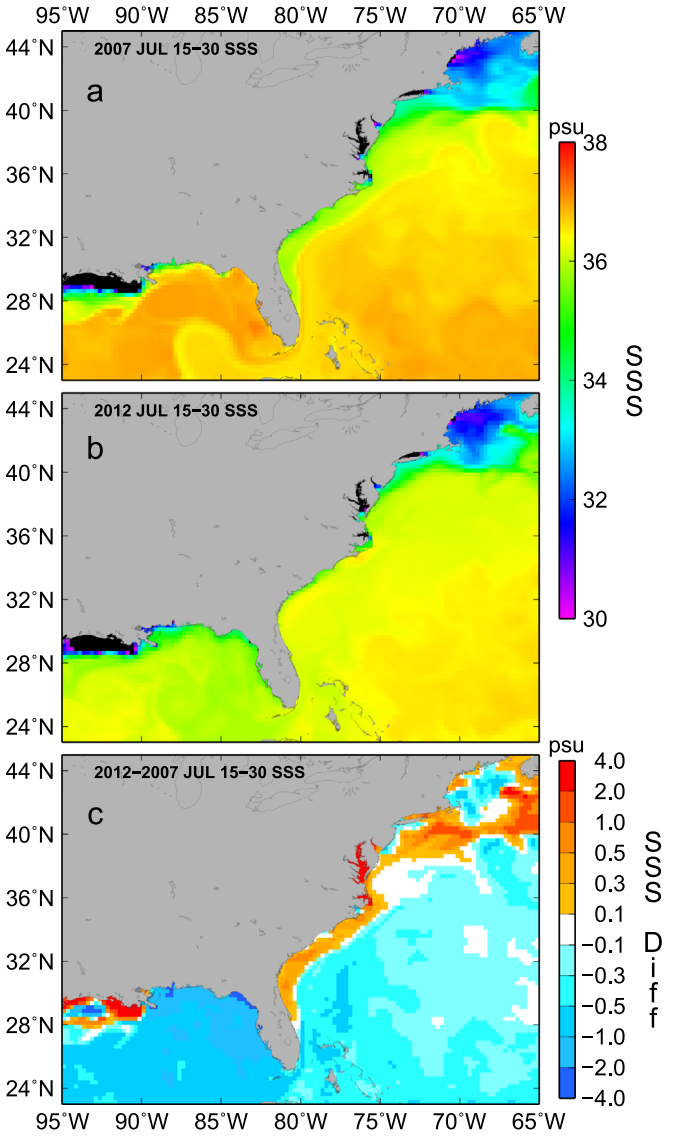

Fig. A2. SSS from RTOFS for 2007 (a), 2012 (b) and difference between 2012 and 2007 (c). The bottom panel can be compared with the differences along the cruise track shown in Fig. 11b.

July 15–30, 2012 and the difference between them, which can be compared with the extrapolated values from the SST differences of cruise observations shown in Fig. 11a. Fig. A2 shows the same information for SSS that can be compared with Fig. 11b. The RTOFS output for the first two weeks in August are very similar to the July output shown. While there are differences on scales that the cruise track does not resolve, the overall pattern is similar, with cooler, fresher water in the Eastern GOM and SE US, and distinctly warmer and saltier waters north of Delaware Bay, with fresher, colder water along line W and in parts of the Gulf of Maine.

Fig. A3 shows the currents in the GOM based on altimetry in July 2007 and July 2012 (www.aviso.altimetry.fr). The 2007 plot shows a well-developed loop current as a source of high Ω_{Ar} waters. In 2012 the loop current does not extend into the GOM. The lower salinities observed on the eastern side of the GOM during GOMECC-2 are attributed to the lack of the northward extension in the loop current in 2012.

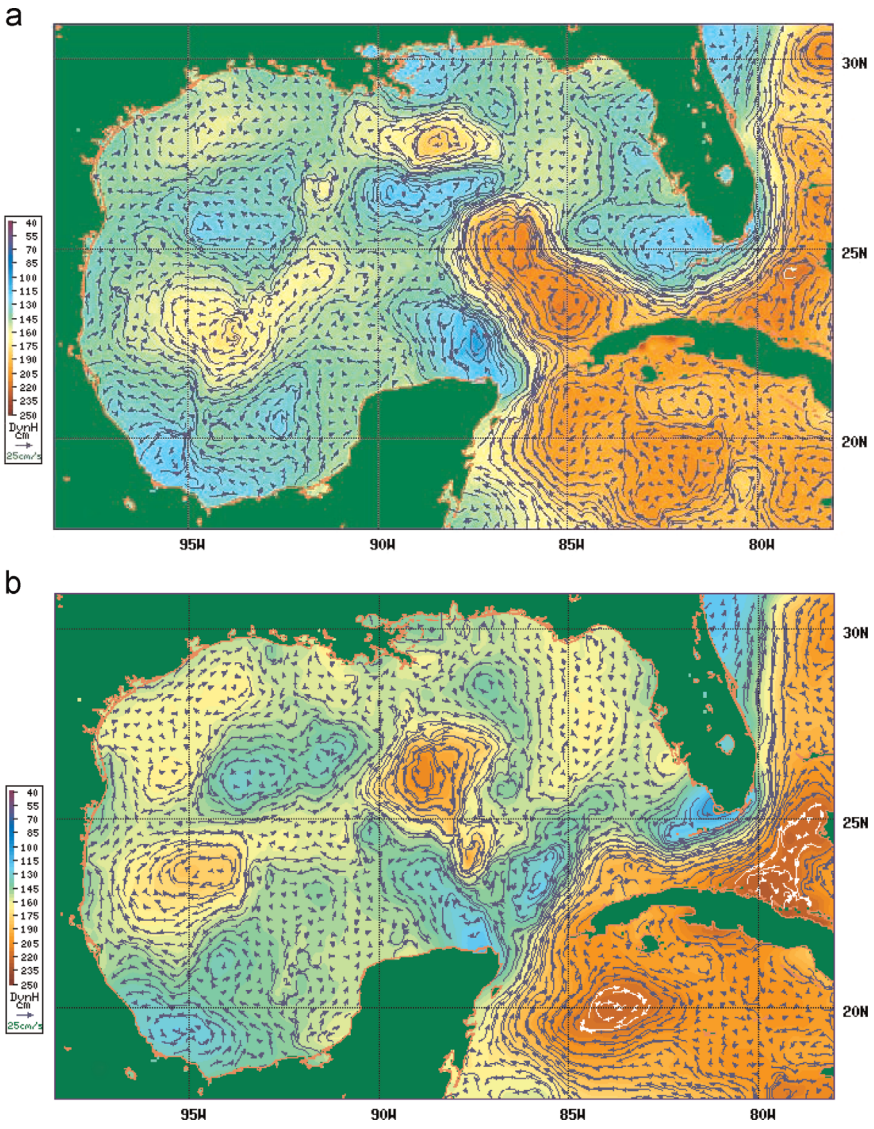

Fig. A3. Surface velocities based on sea surface height (SSH) for July 2007 (top) and July 2012 (bottom),

References

Andersson, A.J., 2014. The oceanic $CaCO_3$ cycle In: Holland, H.D., Turekian, K.K. (Eds.), Treatise on Geochemistry, second edition Elsevier, Oxford, pp. 519–542.

Atkinson, L.P., 1983. Distribution of Antarctic intermediate water over the Blake Plateau. J. Geophys. Res. 88, 4699–4704.

Berner, R.A., Westrich, J.T., Graber, R., Smith, J., Martens, C.S., 1978. Inhibition of aragonite precipitation from supersaturated seawater: a laboratory and field study. Am. J. Sci. 278, 816–837.

Brewer, P.G., Wong, G.T.F., Bacon, M.P., Spencer, D.W., 1975. An oceanic calcium problem. Earth Planet. Sci. Lett. 26, 81–87.

Cai, W.-J., Lohrenz, S.E., 2007. Carbon, nitrogen, and phosphorus fluxes from the Mississippi River and the transformation and fate of biological elements in the riverplume and the adjacent margin In: Liu, K.-K., Atkinson, L., Quiñones, R., Talaue-McManus, L. (Eds.), Carbon and Nutrient Fluxes in Continental Margins: A Global Synthesis. Springer-Verlag, New York.

Cai, W.-J., Hu, X., Huang, W.-J., Wang, Y., Peng, T.-H., Zhang, X., 2010. Alkalinity distribution in the Western North Atlantic Ocean margins. J. Geophys. Res., 115. http://dx.doi.org/10.1029/2009JC005482.

Cai, W.-J., Hu, X., Huang, W.-J., Murrell, M.C., Lehrter, J.C., Lohrenz, S.E., Chou, W.-C., Zhai, W., Hollibaugh, J.T., Wang, Y., Zhao, P., Guo, X., Gundersen, K., Dai, M., Gong, G.-C., 2011. Acidification of subsurface coastal waters enhanced by eutrophication. Nat. Geosci. http://dx.doi.org/10.1038/NGEO1297

Chen, K., Gawarkiewicz, G.G., Lentz, S.J., Bane, J.M., 2014. Diagnosing the warming of the Northeastern U.S. Coastal Ocean in 2012: a linkage between the atmospheric jet stream variability and ocean response. J. Geophys. Res.: Oceans 119, 218–227. http://dx.doi.org/10.1002/2013jc009393.

Clayton, T., Byrne, R.H., 1993. Spectrophotometric seawater pH measurements: total hydrogen ion concentration scale calibration of m-cresol purple and at-sea results. Deep-Sea Res. 40, 2115–2129.

Cooperative Global Atmospheric Data Integration Project, 2013, updated annually. Multi-laboratory Compilation of Synchronized and Gap-filled Atmospheric Carbon Dioxide Records for the Period 1979–2012 (obspack_co2_1_GLOBALVIEW-CO2_2013_v1.0.4_2013-12-23). Compiled by NOAA Global Monitoring Division. Boulder, Colorado, USA. Data product accessed at: http://dx.doi.org/10.3334/OBSPACK/1002

Dickson, A.G., Sabine, C.L., Christian, J.R., 2007. Guide to Best Practices for Ocean CO_2 Measurements. PICES Special Publication 3, 191pp.

Dickson, A.G., 2010a. Part 1: Seawater carbonate chemistry In: Riebesell, U., Fabry, V.J., Hansson, L., Gattuso, J.-P. (Eds.), Guide to Best Practices for Ocean Acidification Research and Data Reporting. Publications Office of the European Union, Luxembourg 260 p.

Dickson, A.G., 2010b. Standards for ocean measurements. Oceanography 23, 34–47.

Emerson, S., Sabine, C., Cronin, M.F., Feely, R., Cullison Gray, S.E., DeGrandpre, M., 2011. Quantifying the flux of $CaCO_3$ and organic carbon from the surface ocean using in situ measurements of O_2, N_2, pCO_2, and pH. Glob. Biogeochem. Cycles 25, GB3008. http://dx.doi.org/10.1029/2010gb003924.

Feely, R.A., Sabine, C.L., Hernandez-Ayon, J.M., Ianson, D., Hales, B., 2008. Evidence for upwelling of corrosive acidified water onto the continental shelf. Science 320, 1490–1492. http://dx.doi.org/10.1126/science.1155676.

Fennel, K., Wilkin, J., Levin, J., Moisan, J., O'Reilly, J., Haidvogel, D., 2006. Nitrogen cycling in the Middle Atlantic Bight: results from a three-dimensional model and implications for the North Atlantic nitrogen budget. Glob. Biogeochem. Cycles 20, GB3007. http://dx.doi.org/10.1029/2005GB002456.

Firing, E., Hummon, J.M., 2010. Ship-mounted acoustic Doppler profilers. In: Hood, E.M., Sabine, C.L., Sloyan, B.M. (Eds.), The GO-SHIP Repeat Hydrography Manual: A Collection of Expert Reports and Guidelines. IOCCP Report no. 14, ICPO Publication Series no 134. Available online at: ⟨http://www.go-ship.org/Hydro

Man.html⟩.
Fratantoni, P.S., Pickart, R.S., 2007. The Western North Atlantic shelfbreak current system in summer. J. Phys. Oceanogr. 37, 2509–2533.
Guo, X., Cai, W.-J., Huang, W.-J., Wang, Y., Chen, F., Murrell, M.C., Lohrenz, S.E., Jiang, L.-Q., Dai, M., Hartmann, J., Lin, Q., Culp, R., 2012. Carbon dynamics and community production in the Mississippi River plume. Limnol. Oceanogr. 57, 1–17. http://dx.doi.org/10.4319/lo.2012.57.1.0001.
Han, G., Chen, N., Ma, Z., 2014. Is there a north-south phase shift in the surface Labrador Current transport on the interannual-to-decadal scale? J. Geophys. Res.: Oceans 119, 276–287.
Harris, K.E., DeGrandpre, M.D., Hales, B., 2013. Aragonite saturation state dynamics in a coastal upwelling zone. Geophys. Res. Lett. 40, 2720–2725. http://dx.doi.org/10.1002/grl.50460.
Hofmann, E., Cahill, B., Fennel, K., Friedrichs, M., Hyde, K., Lee, C., Mannino, A., Najjar, R., O'Reilly, J., Wilkin, J., Xue, J., 2011. Modeling the dynamics of continental shelf carbon In: Carlson, C., Giovannoni, S. (Eds.), Annu. Rev. Mar. Sci. Annu. Rev.,
pp. 93–122. http://dx.doi.org/10.1146/annurev-marine-120709-142740.
Hood, E.M., Sabine, C.L., Sloyan, B.M., 2010. The GO-SHIP Repeat Hydrography Manual: A Collection of Expert Reports and Guidelines. IOCCP Report no 14, ICPO Publication Series no. 134. Available online at: ⟨http://www.go-ship.org/HydroMan.html⟩.
Hu, X., Cai, W.-J., 2011. An assessment of ocean margin anaerobic processes on oceanic alkalinity budget. Glob. Biogeochem. Cycles 25, GB3003. http://dx.doi.org/10.1029/2010GB003859.
Hu, X., Cai, W.-J., 2013. Estuarine acidification and minimum buffer zone – a conceptual study. Geophys. Res. Lett. 40, 5176–5181. http://dx.doi.org/10.1002/grl.51000.
Huang, W.-J., Cai, W.-J., Wang, Y., Lohrenz, S., Murrell, M.C., 2015. The carbon dioxide system on the Mississippi River-dominated continental shelf in the northern Gulf of Mexico- 1: distribution and air-sea CO_2 flux. J Geophys. Res. 120. http://dx.doi.org/10.1002/2014JC010498.
Hydes, D.J., Aoyama, M., Aminot, A., Bakker, K., Becker, S., Coverly, S., Daniel, A., Dickson, A.G., Grosso, O., Kerouel, R., van Ooijen, J., Sato, K., Tanhua, T., Woodward, E.M.S., Zhang, J.Z., 2010. Determination of dissolved nutrients (N, P, Si) in seawater with high precision and inter-comparability using gas-segmented continuous flow analyzers. In:. Hood, E.M, Sloyan, B.M., Sabine, C. (Eds.), GO-SHIP Repeat Hydrography Manual: A Collection of Expert Reports and Guidelines, IOCCP Report no. 14, ICPO Publication Series no. 134, version 1.
Jiang, L.-Q., Cai, W.-J., Feely, R.A., Wang, Y., Guo, X., Gledhill, D.K., Hu, X., Arzayus, F., Chen, F., Hartmann, J., Zhang, L., 2010. Carbonate mineral saturation states along the U.S. East Coast. Limnol. Oceanogr. 55, 2424–2432.
Juranek, L.W., Hamme, R.C., Kaiser, J., Wanninkhof, R., Quay, P.D., 2010. Evidence of O_2 consumption in underway seawater lines: implications for air–sea O_2 and CO_2 fluxes. Geophys. Res. Lett., 37. http://dx.doi.org/10.1029/2009GL040423.
Langdon, C., 2010. Determination of dissolved oxygen in seawater by Winkler titration using the amperometric technique. In: Hood, E.M., Sloyan, B.M., Sabine, C. (Eds.), GO-SHIP Repeat Hydrography Manual: A Collection of Expert Reports and Guidelines. IOCCP Report no. 14, ICPO Publication Series no. 134. Available online at: ⟨http://www.go-ship.org/HydroMan.html⟩.
Lee, T.N., Yoder, J., Atkinson, L.P., 1991. Gulf Stream frontal eddy influence on productivity of the Southeast United States continental shelf. J. Geophys. Res. 96, 22,191–122,205.
Le Hénaff, M., Kourafalou, V.H., Dussurget, R., Lumpkin, R., 2014. Cyclonic activity in the eastern Gulf of Mexico: characterization from along-track altimetry and in situ drifter trajectories. Prog. Oceanogr. 120, 120–138.
Le Quéré, C., Takahashi, T., Buitenhuis, E.T., Rödenbeck, C., Sutherland, S.C., 2010. Impact of climate change and variability on the global oceanic sink of CO_2. Glob. Biogeochem. Cycles 24, GB4007. http://dx.doi.org/10.1029/2009GB003599.
Liu, Q., Charette, M.A., Henderson, P.B., McCorkle, D.C., Martin, W., Dai, M., 2014. Effect of submarine groundwater discharge on the coastal ocean inorganic carbon cycle. Limnol. Oceanogr. 59, 1529–1554. http://dx.doi.org/10.4319/lo.2014.59.5.1529.
Liu, X., Patsavas, M.C., Byrne, R.H., 2011. Purification and characterization of meta-Cresol purple for spectrophotometric seawater pH measurements. Environ. Sci. Technol. 45, 4862–4868.
Lueker, T.J., Dickson, A.G., Keeling, C.D., 2000. Ocean pCO_2 calculated from dissolved inorganic carbon, alkalinity, and equations for $K1$ and $K2$; validation based on laboratory measurements of CO_2 in gas and seawater at equilibrium. Mar. Chem. 70, 105–119.
Manzello, D.P., Enochs, I.C., Musielewicz, S., Carlton, R., Gledhill, D.K., 2013. Tropical cyclones cause $CaCO_3$ undersaturation of coral reef seawater in a high-CO_2 world. J. Geophys. Res., 118. http://dx.doi.org/10.1002/jgrc.20378.
Mehra, A., Rivin, I., 2010. A real time ocean forecast system for the North Atlantic Ocean. Terr. Atmos. Ocean. Sci. 21, 211–228.
Millero, F.J., 1995. Thermodynamics of the carbon dioxide system in the oceans. Geochim. Cosmochim. Acta 59, 661–677.
Mucci, A., 1983. The solubility of calcite and aragonite in seawater at various salinities, temperatures, and one atmosphere total pressure. Am. J. Sci. 283, 780–799.
Patsavas, M.C., Byrne, R.H., Yang, B., Easley, R.A., Wanninkhof, R., Liu, X., 2015. Procedures for direct spectrophotometric measurements of carbonate ion concentrations: Measurements in US Gulf of Mexico and East Coast waters. Marine Chemistry 168, 80–85. http://dx.doi.org/10.1016/j.marchem.2014.10.015.
Pierrot, D., Lewis, E., Wallace, D.W.R., 2006. MS Excel program developed for CO_2 system calculations, ORNL/CDIAC-105a. Carbon Dioxide Information Analysis Center, Oak Ridge National Laboratory, U.S. Department of Energy, Oak Ridge, Tennessee, 10.3334/CDIAC/otg.CO2SYS_XLS_CDIAC105a.
Pierrot, D., Neil, C., Sullivan, K., Castle, R., Wanninkhof, R., Lueger, H., Johannson, T., Olsen, C.E., Feely, R.A., Cosca, C.E., 2009. Recommendations for autonomous underway pCO_2 measuring systems and data reduction routines. Deep-Sea Res. II 56, 512–522.
Rabalais, N.N., Cai, W.-J., Carstensen, J., Conley, D.J., Fry, B., Hu, X., Quiñones-Rivera, Z., Rosenberg, R., Slomp, C.P., Turner, R.E., Voss, M., Wissel, B., Zhang, J., 2014. Eutrophication-driven deoxygenation in the coastal ocean. Oceanography 27, 172–183.
Reynolds, R.W., Smith, T.M., Liu, C., Chelton, D.B., Casey, K.S., Schlax, M.G., 2007. Daily high-resolution blended analyses for sea surface temperature. J. Clim. 20, 5473–5496.
Rubin, S.I., Key, R.M., 2002. Separating natural and bomb-produced radiocarbon in the ocean: the potential alkalinity method. Glob. Biogeochem. Cycles 16, 1105. http://dx.doi.org/10.1029/2001GB001432.
Salisbury, J.E., Green, M., 2008. Episodic acidification of coastal waters. EOS Trans. 89, 513–514.
Schlitzer, R., 2014. Ocean Data View, ⟨http://odv.awi.de⟩.
Seitzinger, S.P., Giblin, A.E., 1996. Estimating denitrification in North Atlantic continental shelf sediments. Biogeochemistry 35, 235–260.
Signorini, S.R., Mannino, A., Najjar, R.G., F.M.A., M., Cai, W.-J., Salisbury, J., Wang, Z. A., Thomas, H., Shadwick, E.H., 2013. Surface ocean pCO_2 seasonality and sea-air CO_2 flux estimates for the North American East Coast. J. Geophys. Res., 118. http://dx.doi.org/10.1002/jgrc.20369.
Takahashi, T., Sutherland, S.C., Wanninkhof, R., Sweeney, C., Feely, R.A., Chipman, D. W., Hales, B., Friederich, G., Chavez, F., Sabine, C., Watson, A., Bakker, D.C.E., Schuster, U., Metzl, N., Inoue, H.Y., Ishii, M., Midorikawa, T., Nojiri, Y., Koertzinger, A., Steinhoff, T., Hoppema, M., Olafsson, J., Arnarson, T.S., Tilbrook, B., Johannessen, T., Olsen, A., Bellerby, R., Wong, C.S., Delille, B., Bates, N.R., de Baar, H.J.W., 2009. Climatological mean and decadal change in surface ocean pCO_2, and net sea-air CO_2 flux over the global oceans. Deep -Sea Res. II, 554–577. http://dx.doi.org/10.1016/j.dsr2.2008.12.009.
Takahashi, T., Broecker, W.S., Langer, S., 1985. Redfield ratio based on chemical data from isopycnal surfaces. J. Geophys. Res. 90, 6907–6924.
Takahashi, T., Olafsson, J., Goddard, J.G., Chipman, D.W., Sutherland, S.C., 1993. Seasonal variation of CO_2 and nutrients in the high-latitude surface oceans: a comparative study. Glob. Biogeochem. Cycles 7, 843–878.
Waldbusser, G.G., Hales, B., Langdon, C.J., Haley, B.A., Schrader, P., Brunner, E.L., Gray, M.W., Miller, C.A., Gimenez, I., 2015. Saturation-state sensitivity of marine bivalve larvae to ocean acidification. Nat. Clim. Change 5, 273–280. http://dx.doi.org/10.1038/nclimate2479.
Wang, Z.A., Wanninkhof, R., Peng, T.-H., Cai, W.-J., Hu, X., Huang, W.-J., Byrne, R., 2013. The marine inorganic carbon system along the Gulf of Mexico and Atlantic coasts of the United States: insights from a transregional coastal carbon study. Limnol. Oceanogr. 58, 325–342. http://dx.doi.org/10.4319/lo.2013.58.1.0325.
Wanninkhof, R., Thoning, K., 1993. Measurement of fugacity of CO_2 in surface water using continuous and discrete sampling methods. Mar. Chem. 44, 189–205.
Wanninkhof, R., Park, G.-H., Takahashi, T., Sweeney, C., Feely, R., Nojiri, Y., Gruber, N., Doney, S.C., McKinley, G.A., Lenton, A., Le Quéré, C., Heinze, C., Schwinger, J., Graven, H., Khatiwala, S., 2013. Global ocean carbon uptake: magnitude, variability and trends. Biogeosciences 10, 1983–2000.
Wanninkhof, R., Barbero, L., Baringer, M., Byrne, R., Cai, W.-J., Langdon, C., Lohrenz, S., Salisbury, J., Zhang, J.-Z., 2014. Dissolved Inorganic Carbon, Total Alkalinity, pH, fugacity Of Carbon Dioxide, and Other Variables from Profile and Surface Observations Using CTD, Niskin bottle, Flow Through Pump and Other Instruments from the Ronald H. Brown in the Gulf of Mexico and East Coast of the United States from 2012-07-22 to 2012-08-13, NODC Accession 0117971, doi: 10.7289/V5542KJ.
Wittmann, A.C., Portner, H.-O., 2013. Sensitivities of extant animal taxa to ocean acidification. Nat. Clim. Change 3, 995–1001.
Zeebe, R.E., Wolf-Gladrow, D., 2001. CO_2 in Seawater: Equilibrium, Kinetics, Isotopes. Elsevier Oceanography Series 65, Amsterdam.
Zhang, J., Cowie, G., Naqvi, S.W.A., 2013. Hypoxia in the changing marine environment. Environ. Res. Lett. 8, 015025. http://dx.doi.org/10.1088/1748-9326/8/1/015025.
Zhang, J.-Z., Berberian, G.A., September 1997. Determination of dissolved silicate in estuarine and coastal waters by gas segmented continuous flow colorimetric analysis. Methods for the Determination of Chemical Substances in Marine and Estuarine Environmental Matrices, 2nd edition, EPA/600/R-97/072.
Zhang, J.-Z., Fischer, C., Ortner, P.B., 2000. Comparison of open tubular cadmium reactor and packed cadmium column in automated gas-segmented continuous flow nitrate analysis. Int. J. Environ. Anal. Chem. 76 (2), 99–113.
Zhang, J.-Z., Fischer, C., Ortner, P.B., 2001. Continuous flow analysis of phosphate in natural waters using hydrazine as a reductant. Int. J. Environ. Anal. Chem. 80 (1), 61–73.